UNIVERSITY OF CALIFORNIA

Los Angeles

Exploring Potential Molecular Platforms for Quantum Technology

A dissertation submitted in partial satisfaction
of the requirements for the degree
Doctor of Philosophy in Department of Physics and Astronomy

by

Changling Zhao

2023

ABSTRACT OF THE DISSERTATION

Exploring Potential Molecular Platforms
for Quantum Technology

by

Changling Zhao
Doctor of Philosophy in Department of Physics and Astronomy
University of California, Los Angeles, 2023
Professor Wesley C. Campbell, Chair

In recent years, there has been significant progress in the field of quantum information processing and quantum sensing. Researchers have been actively exploring new quantum systems that possess high accuracy, scalability, and compatibility with other systems. The focus of this thesis is to examine various molecular systems that hold promise for quantum sensing and information processing applications.

We report a ferrocene-supported ytterbium based complex ((thiolfan)YbCl(THF), thiolfan = 1,1'-bis(2,4-di-tert-butyl-6-thiomethylenephenoxy)ferrocene) that exhibits an isolated ultranarrow absorption linewidth in solution at room temperature with a full width at half maximum (FWHM) of (151 $\pm$ 1) GHz. A detailed absorption spectroscopy analysis from room temperature (RT) to 5 K and emission spectroscopy allow us to assign the narrow near infrared (NIR) transitions to atom-centered *f-f* transitions. Zeeman spectroscopy and electron paramagnetic resonance measurement help us to determine the dominant quantum numbers and Landé g-factors of the ground and excited states. A combination of density functional theory and multireference methods match experimental transition energies and

oscillator strengths, providing insights into the role of spin-orbit coupling and asymmetric ligand field in enhancing absorption and pointing toward molecular design principles that create well-protected yet observable electronic transitions in lanthanide (Ln) complexes.

We demonstrate that the ultranarrow linewidth of this system allows for magnetic field imaging and magnetic field sensing down to Earth scale, which we term an "atom-like molecular sensor" (ALMS). Furthermore, by optically depleting some population, we are able to selectively address the burned spectral hole with a FHWM of 99 kHz, paving the way for optical state preparation and readout of ground state coherence in this liquid molecular system.

In addition, we also describe our efforts in building surface-based molecular systems for quantum information and we find that the sensitivity is limited by scatters from the substrate.

Overall, our results suggest that molecular systems like ALMS may have great potential for quantum sensing and information applications.

The dissertation of Changling Zhao is approved.

Eric R. Hudson

Anastassia N. Alexandrova

Justin R. Caram

Wesley C. Campbell, Committee Chair

University of California, Los Angeles

2023

To my family, friends, people who I love and people who love me.

TABLE OF CONTENTS

LIST OF FIGURES

LIST OF TABLES

ACKNOWLEDGMENTS

First and foremost, I would like to sincerely thank my advisor, Wes Campbell, for his invaluable guidance and mentorship throughout my journey as a physicist. Wes shaped my understanding of the field and have encouraged me to explore new ideas. He always supports us to choose approaches that we think is the most interesting and promising and learn from both successes and failures. He taught me that failures are not a bad thing especially if I can learn from it what is not working and what gives the current limitations. I am grateful to have had Wes as my advisor during my PhD research, and the lessons I have learned from him will undoubtedly benefit me for the rest of my life.

I am also deeply grateful to my committee members: Justin Caram, Anastassia Alexandrova, and Eric Hudson. Our weekly project meetings provided a platform for fruitful discussions, and I have greatly enjoyed gaining insights from both the chemist's and physicist's perspectives.

I consider myself fortunate to have collaborated with a team of brilliant individuals: Ashley Shin, Claire Dickerson, Yi Shen, Barry Li, Yongjia He, Han Guo, and Timothy Atallah. Chapters 1, 2, and 3 of this work are adapted from the papers we wrote together [28]. Ashley's boundless energy and constant support have been invaluable to both the experiments and my personal life. Claire's expertise as a theorist has greatly aided my understanding of theoretical concepts as an experimentalist. Yi, our hero in synthesis, has worked tirelessly in synthesizing and characterizing the samples, including handling the delicate samples in the glove box. I am also grateful for the mentorship provided by the postdocs, Han and Timothy. The future of the project is in excellent hands with the contributions of the younger graduate students, Barry and Yongjia.

I extend my gratitude to the welcoming AMO community at UCLA. I have learned immensely from individuals such as Xueping Long and Scarlett Yu, who helped me set up the surface OCC project (Chapter 6) when I first joined the group. Anthony Ransford, Conrad

Roman, and Gary Chen have always been available to lend their assistance. Guozhu Zhu and Guanming Lao have provided kind support to my Yb complex project. I am also grateful for the help from Thomas Dellaert, Patrick McMillan, and Hassan Farhat, the esteemed atomic physicists and ion trappers. I cannot forget the memorable experiences shared with Matthew Boguslawski and his pink electric skateboard, Randy Putnam and his chess quizzes, Sami Khamis and his lovely cats, and Grant Mitts and his love for pineapples. There are many more names I can list. The members of Wes Campbell's group, Eric Hudson's group, and Paul Hamilton's group have collectively made my time at UCLA truly delightful.

To my friends and roommates, Yixuan Xu, Yanan Yu, and Jia Han, I am grateful for their companionship and support as I adjusted to this foreign environment. I have cherished moments spent engaging in various activities with Yixuan. Together we learned swimming, tennis, and snowboarding. Their company and emotional support I received from friends who are physically distant have been crucial in helping me navigate challenging times.

Lastly, I would like to express my heartfelt appreciation to my family for their unwavering support throughout my life. They have consistently encouraged me to pursue my passions, and I know they will stand by my side no matter what challenges I face. Our video chats during my commute have been a source of joy and comfort. Being far away from them for an extended period has made me miss them very much.

VITA

2013-2017 B.A. (Applied Physics) University of Science and Technology of China

2017-2018 M.S. (Physics) University of California, Los Angeles

PUBLICATIONS

Shin, A. J.†, **Zhao, C.**†, Shen, Y.†, Dickerson, C. E.†, Li, B, Bim, D., Alson, L. K., Atallah, T., Diaconescu, P. L., Alexandrova, A. N., Campbell, W. C., Caram, J. R. "Toward liquid cell quantum sensing: Ytterbium complexes with ultra-narrow absorption", *ChemRxiv. Cambridge: Cambridge Open Engage* (2022)

Guo, H., Dickerson, C. E., Shin, A. J., **Zhao, C.**, Atallah, T. L., Caram, J. R., Campbell, W. C., Alexandrova, A. N. "Surface chemical trapping of optical (thiolfan)YbClcycling centers", *Physical Chemistry Chemical Physics*, **23**, 211-218 (2021)

CHAPTER 1

Introduction

The field of quantum information processing, quantum computing and quantum sensing have been widely studied with ultracold, gas-phase atoms or ions[1, 2, 3], superconducting circuits[4, 5, 6], photonic integrated circuits[7, 8, 9] and quantum dots and dopants in solids[10, 11, 12]. The core quantum unit is the qubit, which can be any system with two well-defined states $|0\rangle$ and $|1\rangle$ that can be used for state preparation, manipulation and selectively readout. Atomic systems are well-suited for this due to their extremely narrow-band optical cycling transitions[13]. Molecular systems, on the other hand, do not naturally possess this desirable property, as they can decay into a vast number of vibrational states. However, molecular systems offer the unique opportunities to design and engineer things in a way that is not possible with atoms. It has the modularity to functionalize molecules with specific properties and chemically alter them independently. This opens the possibility of designing a molecule in which different parts can serve distinct functions, such as optical cycling, storage, and gate operation.

Lanthanide-based molecules are worth investigating because their $4f$ electrons are shielded by the $5s^2$ and $5p^6$ orbitals, which makes them scarcely available for covalent interaction with the ligands[14]. Additionally, they exhibit strong strong spin-orbital (SO) coupling where the SO splittings are larger than crystal/ligand field splittings, unlike $3d$-transition metal ions which have relatively weak spin-orbit coupling compared to crystal/ligand field. As a result, the orbital contribution to the magnetic moment is large and unquenched in Ln-based molecules, and ligand field effects can be regarded as a small but significant perturbation

[15]. This makes Ln-based molecules good candidate for single molecular magnet[15][16] and molecular spins[17]. In this work, we investigate a novel Ln-based molecule and explore its potential applications in magnetic field sensing and quantum information processing.

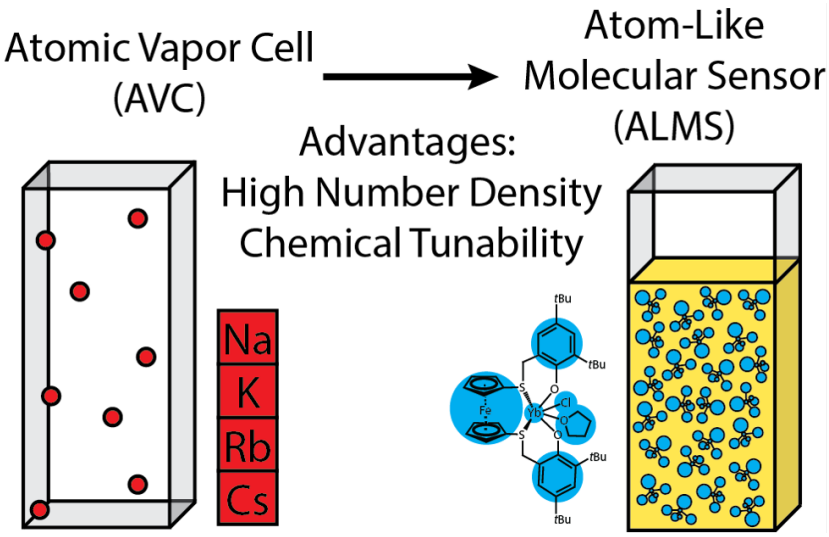

Figure 1.1: AVC vs ALMS. Ref [28]

Atomic vapor cells (AVCs) are among the most sensitive and widely deployed methods of detecting magnetic fields, with numerous applications in fields such as nuclear magnetic resonance (NMR) and magnetic resonance imaging (MRI)[18][19]. Typically consisting of vaporized alkali-metal atoms (such as Rb) contained within a sealed glass container, AVCs employ lasers to optically pump the spins, and measure polarization rotation of an orthogonal probe as an indicator of magnetic field. AVC magnetometers have reached extraordinary sub-femtotesla sensitivity in a relatively compact form[20].

The established limit of AVC sensitivity for magnetic fields is set by:

$$\Delta B \approx \frac{1}{g\mu_{\mathrm{B}}} \frac{\hbar}{\sqrt{N\tau T}} \tag{1.1}$$

Where ΔB is the uncertainty in the measured magnetic field, g is the ground state Landé factor, μ_{B} is the Bohr magneton, $\hbar$ is the Planck's constant, N is the number of atoms, τ is the coherence time, and T is the measurement duration[18]. In AVCs, higher sensitivity can be

achieved by increasing N, which can be accomplished by raising the temperature. However, this also results in reduced coherence time due to increased collision-based dephasing[18, 20, 21]. Our goal is to develop a denser system that preserves coherence. Liquid or solid systems can reach a density that is 6 orders of magnitude higher than gas phase AVCs. But we cannot directly put metal atoms into liquid or solid systems because collisions in liquid system and local disorders in solid systems will significantly broaden the linewidth to THz or even worse. If we want to do things in liquid or solid state, we need to find a way to protect this atomic transition. And our idea is to implement the atom into a molecule so that the surrounding atoms or ligand can act like an armor to protect it from collisions and environmental fluctuations. However, it is crucial to carefully select the appropriate metal center and ligand structure to ensure that the electric and magnetic fields generated by the surrounding ligands do not disrupt the metal center's transition. Or in other words, the atomic transition should be preserved under ligand field interactions. We are most interested in designing a liquid analogue to an AVC, such as an atomic-like molecular sensor (ALMS). It would leverage atomic-like transitions while minimizing drawbacks by accessing much higher number densities. If narrow linewidths can be maintained in solution, the number density limits of AVCs could be overcome.

We chose the f-centered transitions in trivalent lanthanide complexes as a potential testbed for the applicability of atomic physics technologies in condensed-phase chemistry. Our focus is on trivalent Yb, which has an electron configuration of $4f^{13}$ (one electron is lacking to fill the $4f$ shell). The ground and excited states of gas phase Yb^{3+} are $^2F_{7/2}$ and $^2F_{5/2}$, respectively. In the gas phase, these transitions are E1 (electric dipole) forbidden, interacting only through M1 (magnetic dipole). However for molecules, the ligand environment mixes the states, which allows us to open small electric dipole transitions among f-electron configurations and create atom-centered transitions with non-negligibl oscillator strengths[22][23]. As a result, these complexes display near-infrared absorption bands, which retain extremely narrow yet measurable linewidths even in condensed phase environments[24][25]. Solubiliza-

tion allows for a high number density of these species in a set volume, reaching upwards of 10^{19} molecules per cm^3 (i.e. 10 mM), a value eight orders of magnitude greater than the average density of their AVC counterparts[26][27].

In Chapter 2, we showcase an unprecedented ultranarrow (151 GHz) optical absorption feature achieved in a room temperature, molecular lanthanide system – a suggestive first step to liquid-based quantum sensing. In Chapter 3, we will demonstrate magnetic field sensing with this liquid system through direct transmission of circularly polarized light, capable of detecting the Earth's magnetic field ($\sim$0.25 G). This paves the way for a novel liquid-based magnetometry method. Chapter 4 delves into the even narrower 100 kHz spectral hole burning linewidth, providing an exciting glimpse of the potential for state preparation and measurement. Chapter 5 explores the future directions of this novel liquid molecular system, including electric field sensing, real qubit manipulation, expanding the ultranarrow family, and surface implementation. Chapter 6 offers a preliminary demonstration of surface system.

CHAPTER 2

Ultranarrow linewidth of Yb-based molecules

In quantum technology (such as atomic vapor cells used in precision magnetometry), the energetic disorder caused by a fluctuating liquid environment can undermine the precise control required for coherence-based sensing. To overcome these fluctuations, a protected quantum subspace is needed that only weakly interacts with the local environment. Here we show a ferrocene-supported ytterbium complex ((thiolfan)YbCl(THF), thiolfan = 1,1'-bis(2,4-di-tert-butyl-6-thiomethylenephenoxy)ferrocene) that exhibits an extraordinarily narrow optical absorption linewidth in solution at room temperature with a full-width at half-maximum of 151±1 GHZ.

2.1 Experimental setup

The molecule (thiolfan)YbCl(THF) and other variants (shown in Figure 2.1) are synthesized by Yi Shen (Paula Diaconescu group in UCLA chemistry department). The detailed synthesis method can be found in Ref [28]. The Yb(III) complex, (thiolfan)YbCl, was synthesized by deprotonating H_2(thiolfan), followed by a reaction with $YbCl_3(THF)_3$ (THF = tetrahydrofuran) at -78°C. The solid-state molecular structure revealed a dinuclear compound, $[(\text{thiolfan})\text{YbCl}]_2$, where the sample was crystallized out of toluene and has two ytterbium centers bridged by two chlorides. However, we note that the spectral measurements in the following sections were performed after dissolving the sample in THF or 2-MeTHF (2-Methyltetrahydrofuran), in which the compound exists as a monomer. The monomer sample is coordinated to the solvent molecules, specifically with THF in the solution phase and 2-

MeTHF in the glass phase. NMR, elemental analysis (EA), magnetic properties measurement with superconducting quantum interference device (SQUID), diffusion ordered spectroscopy (DOSY) and other characterization analyses were done by Yi Shen to confirm the structure of this molecule. A titration of $[(\text{thiolfan})\text{YbCl}]_2$ in toluene with small additions of THF was done by Ashley Shin (from Justin Caram group in UCLA chemistry department) to support that the sample is a THF coordinated monomer when dissolved in THF. Figure 2.1 shows the THF coordination.

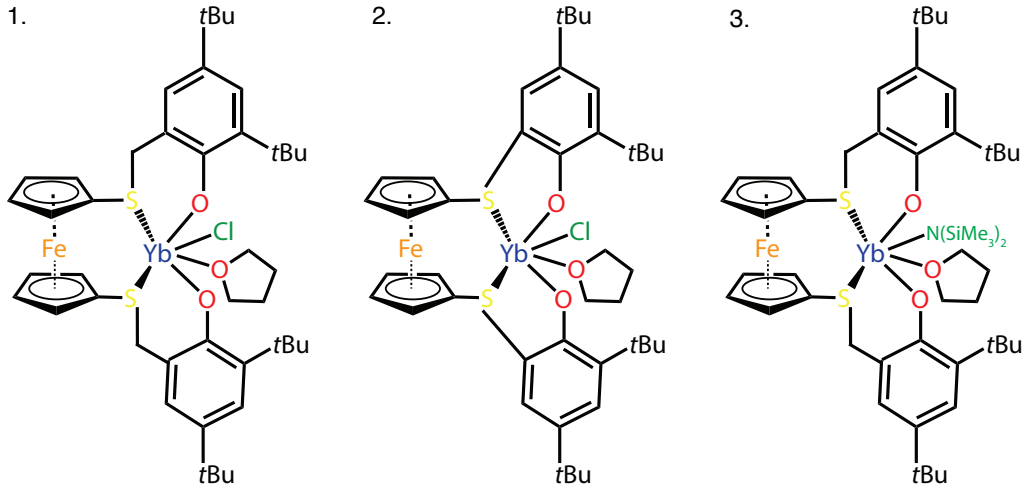

Figure 2.1: The structure of Yb based molecules investigated in this work. 1: (thiolfan)YbCl. 2: (thiolfan)*YbCl. 3: (thiolfan)$\text{YbN}(\text{SiMe}_3)_2$. tBu or terttutyl ligands make the molecule soluble in organic solvents.

A high-resolution transmission/absorption spectrum of the sample was measured with a tunable narrow band CW laser (M Squared SolsTis Ti:Sapph laser). The laser beam was split into two paths by a polarizing beam splitter (PBS), with one beam measuring the absorption of the solvent and the other measuring the absorption of the sample. A quarter wave-plate (QWP) was used to change the polarization of the laser beam, enabling polarization-dependent absorption spectrum measurements. Two permanent magnets ($1.35 \times 1.35 \times 2.35$ in N52 grade magnet from Magneto Inc., capable of creating a static magnetic field up to 0.4

T) were used to induce Zeeman splitting. The magnetic field was measured using a gaussmeter (Lakeshore 410). The translational stage allowed us to control the distance between the magnet and the sample and to vary the strength of the magnetic field at the sample's location. The setup is shown in Figure 2.2.

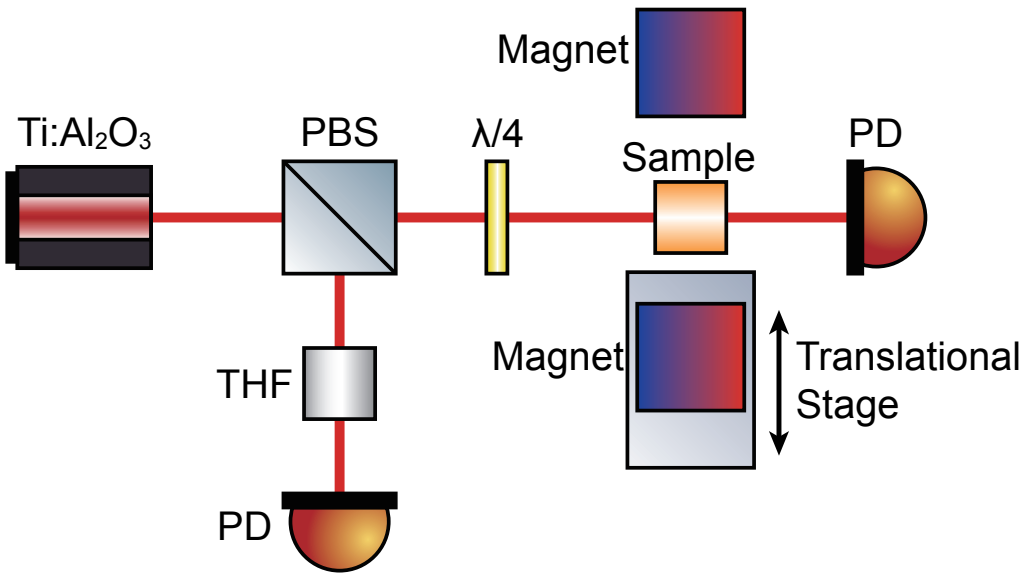

Figure 2.2: Optical setup for the high-resolution transmission/absorption spectrum measurement with various static magnetic field at room temperature.

Cold temperature experiments were conducted with (thiolfan)YbCl in 2-MeTHF because it facilitates the formation of a good glass below around 120 K, whereas frozen THF is more opaque[29]. The sample was loaded into a 0.2 mm cuvette and then placed in the cryostat (ST-100 continuous flow optical cryostat system from Lake Shore Cryotronics) by Yi Shen in a glove box to prevent the sample from degrading. Then, a UV-Vis spectrum was taken with (model number) to confirm the sample's viability. The freezing point of our sample in 2-MeTHF is around 120 K. Liquid nitrogen (LN_2) was used to cool the sample to 77 K and liquid helium (LHe) was used to cool the sample to 5 K.

2.2 Absorption spectroscopy

2.2.1 Room temperature absorption spectra

Figure 2.3 is the UV-Vis spectrum of sample 1 (4 mM (thiolfan)YbCl(THF)) taken by Ashley Shin. Absorbance is the logarithm of one over transmission. There are four main peaks resolved. I is the 400 nm to 600 nm broad band visible absorption which is from the ligands. II - IV are three relatively weak absorbing transitions from 880 nm to 980 nm (II peaks at 900 nm, III peaks at 925 nm, IV peaks at 980 nm) which we believe are from the Yb^{3+} center (Section 2.6). Our primary focus is on the narrow transition denoted IV, which shares a similar energy gap to that of the gas phase Yb^{3+} ion (which is at 979 nm).

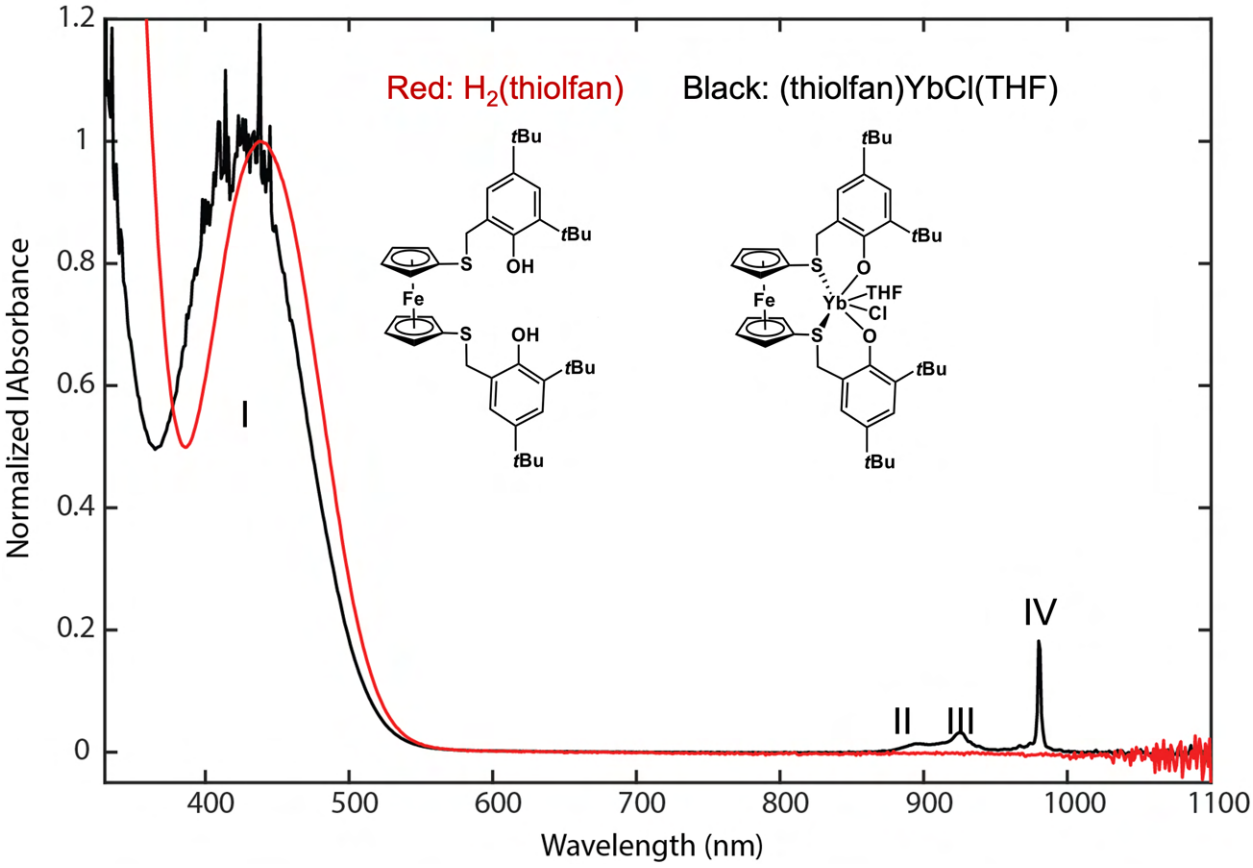

Figure 2.3: UV-Vis spectrum of (thiolfan)YbCl(THF) in THF compared with its ligand. This spectrum is taken with 4 mM sample dissolved in THF at room temperature.

Conventional UV-Vis spectrometers lack the resolution necessary to quantify sub THz linewidths in the near infrared. Therefore, we utilize a narrowband, continuous-wave Ti:sapphire laser to scan the transmission (Figure 2.2). The spectrum is shown in the following figure 2.4. The sample is 4 mM (thiolfan)YbCl(THF) (sample 1 in Figure 2.1). The measured spectrum is fitted with a Lorentzian function with FWHM 151±1 GHz.

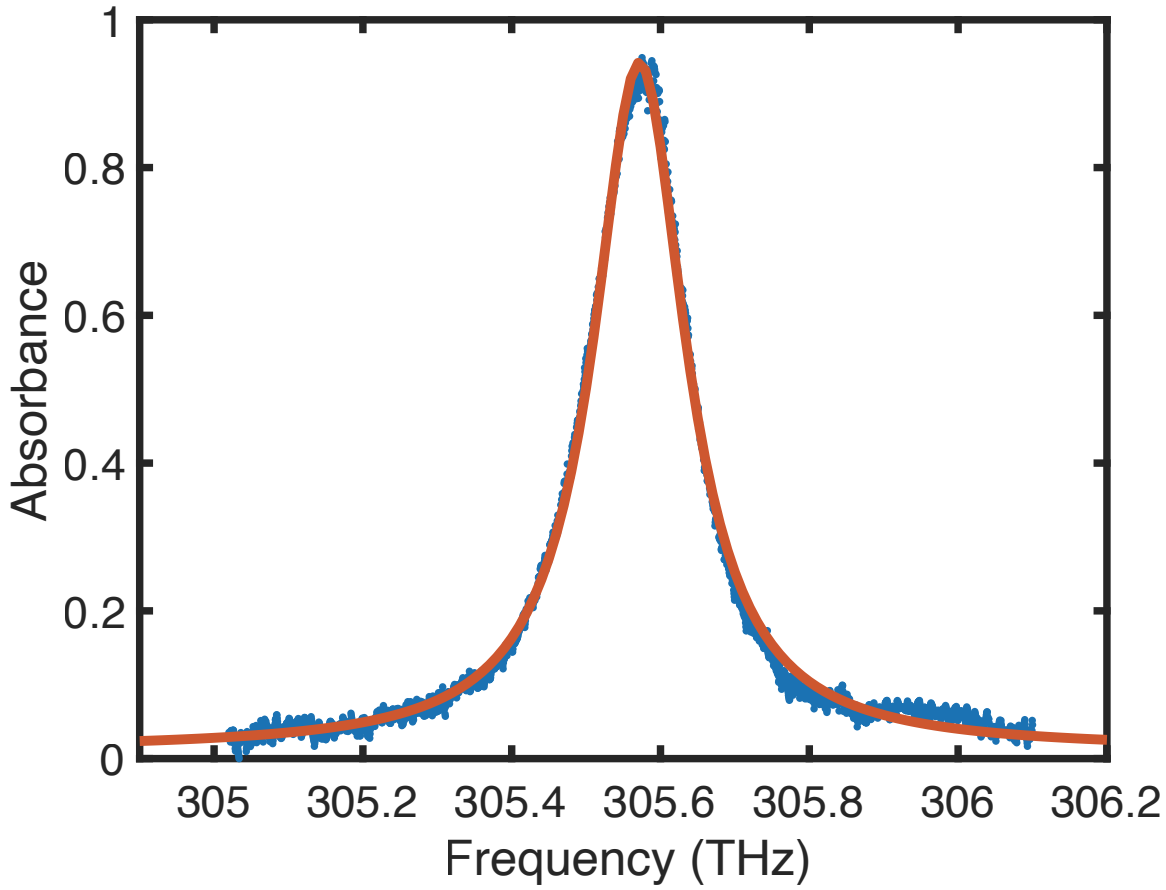

Figure 2.4: Absorption spectrum of (thiolfan)YbCl in THF. FWHM = 151±1 GHz.

This is extremely narrow considering that it is a molecular system with has tremendous vibrational and rotational states and it is a liquid system with inevitable collisions and

molecular motions. For example, dye molecules typically have optical absorption linewidths of hundreds of THz linewidth at room temperature[30]. This molecule displays a narrower room temperature solution linewidth compared to many similar systems in the condensed phase, optical cavities, and cryogenic temperatures. (A linewidth comparison table can be found in the SI of [28]. The following table 2.1 only shows part of it.) Our central hypothesis for the correlation between molecular structure and the ultranarrow linewidth is that the rigidity of the ferrocene backbone in the supporting ligand sphere minimize inhomogeneous broadening and f/d orbital coupling, respectively. For example, Yb(trensal) is a compound with a high degree of magnetic anisotropy and well-defined optical features that shows a linewidth of 1.1 THz[31], roughly an order of magnitude broader than (thiolfan)YbCl(THF). Contrary to our system, Yb(trensal) shows many absorption features assigned to other spin-orbit transitions and vibrations, and a large apparent Stokes shift, suggesting a more mixed and "molecular" electronic structure in comparison. Even Yb^{3+} doped crystals at 4 K show a larger linewidth of 0.87 THz[32], almost 6 times broader than (thiolfan)YbCl(THF), attributed to inhomogeneous crystal environments and phonon coupling[33][34]. To the best of our knowledge, our thiolfanYbCl(THF) compound exhibits the narrowest optical absorption linewidth among room temperature liquid molecular systems.

Name	Ion transition	FWHM	Phase	Temp.	Ref.
(thiolfan)YbCl(THF)	Yb^{3+} $^2F_{7/2}$ - $^2F_{5/2}$	0.15 THz	Solution	RT	This work
[$YbL_2(OTf)_2$](OTf)	Yb^{3+} $^2F_{7/2}$ - $^2F_{5/2}$	6 THz	Solution	4 K	[35]
Yb^{3+} Helicene	Yb^{3+} $^2F_{7/2}$ - $^2F_{5/2}$	0.87 THz	Crystal	4 K	[32]
Yb^{3+} Trensal	Yb^{3+} $^2F_{7/2}$ - $^2F_{5/2}$	1.1 THz	Crystal	RT	[31]
Eu^{3+} in $HClO_4$	Eu^{3+} $^7F_0$ - $^5D_1$	2.7 THz	Solution	RT	[36]
Yb^{3+} in YVO	Yb^{3+} $^2F_{7/2}$ - $^2F_{5/2}$	200 MHz	Crystal	40 mK	[37]

Table 2.1: Linewidth comparison of Ln-based systems.

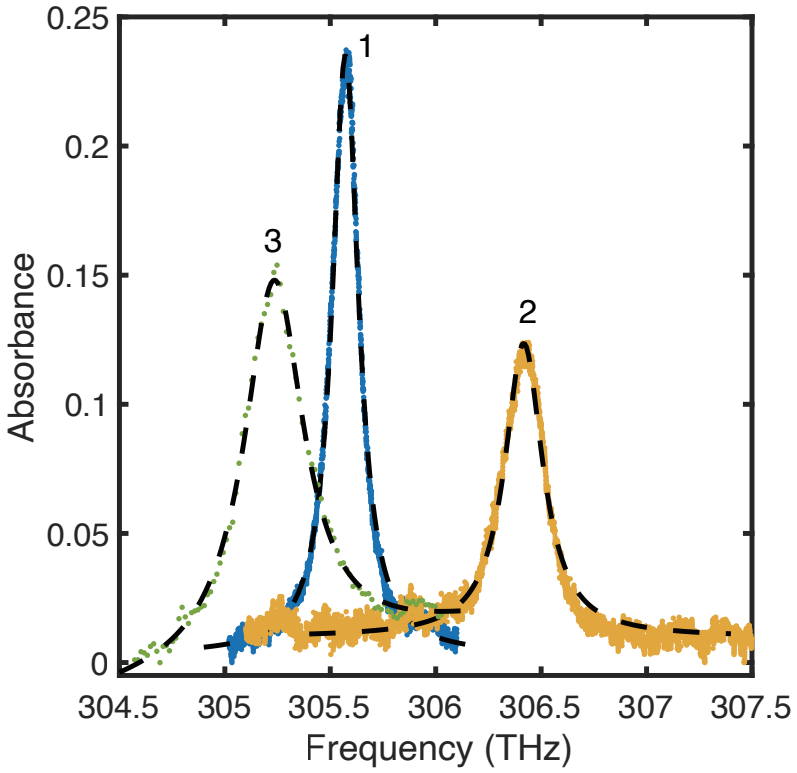

Figure 2.5: Absorption spectra of three variants of Yb based complexes in THF. 1: (thiolfan)YbCl with FWHM 151±1 GHz. 2: (thiolfan)*YbCl with FWHM 218±2 GHz. 3: (thiolfan)YbN($SiMe_3$)$_2$ with FWHM 346±2 GHZ.

We investigated the relationship between this ultranarrow linewidth and molecular geometry by synthesizing two variants of (thiolfan)YbCl(THF) with slightly different ligand environments (Figure 2.1), one variant with one fewer carbon connecting the ferrocene and phenoxy moieties (Figure 2.1 2) and another variant with -Cl replaced by -N($SiMe_3$)$_2$ (Figure 2.1 2). A high-resolution scan of the transmission of the three variants indicates that the linewidth of this transition is preserved (Figure 2.5), likely because the rigidity of the ferrocene backbone provides protection of the radiative transition from other sources of line broadening. The amide variant 3 has a FWHM of 346±2 GHZ, while 2 has a FWHM of 218±2 GHz, which are both comparable to the 151±1 GHz linewidth of 1. Although the

exact broadening mechanism is unknown, the slight increase in linewidth is mostly likely due to the shorter carbon bridge of 2 changing metal-ligand coupling, and the strong ligand field of the amide group in 3 contributing to the inhomogeneous broadening of the metal transition. The important observation, however, is that all three ytterbium complexes display extremely narrow linewidths in solution, despite shifts in the primary transition energy that can be attributed to slight deviations in the coordination geometry. Therefore, the original thiolfan ligand preserves the narrowest Yb^{3+} transition linewidth, while minimizing the ligand effects relative to the ground spin-orbit transition.

2.2.2 Cold temperature absorption spectra

To investigate temperature dependent contributions to the linewidth broadening, we did a series of absorption measurement with temperature from room temperature to 5 K. Sample we used was 30 mM (thiolfan)YbCl in 2-MeTHF in a 0.2 mm cuvette. Thin cuvette and 2-MeTHF solvent help to form a good transparent glass as we cool down the sample. Figure 2.6 a shows the measured absorption spectrum at various temperature from 320 K to 5 K. Experiments were done in two runs, one with LN_2 as cooling agent and one with LHe as cooling agent to cover the full 5 - 320 K range.

We find that the absorption feature at around 980 nm (transition IV) remains unimodal at cryogenic temperatures, with a slight narrowing in peak FWHM and red shift in peak energy as the temperature decreases to 5 K. It should be noted that the sample freezes into a glass form below 120 K. Thus, the spectra in Figure 2.6 reflect the optical behavior of the sample in disordered glass at varying temperatures, therefore more closely reflecting its behavior dissolved in solution, as opposed to a solid or crystal. As we cool down the sample, the sample volume decreases so distance dependent intermolecular interactions changes accordingly. This could be why there is a 70 GHz peak maximum shift from room temperature to 5 K (Figure 2.6 b). Aside from transition energy shift, we also notice the linewidth narrows by around 30 - 40 GHz as we cool down. This indicates that thermal effects like

molecular velocity, collision frequency and thermal population on vibrational and rotational states only contributes a small portion to the 151 GHz linewidth. Considering fluctuations and local disorders in the liquid and glass environment, we believe the peak is dominated by inhomogeneous broadening (A more detailed discussion on broadening mechanisms is in Section 4.3). That is, individual chromophores may have slightly different geometries and environment and thus varying transition energies. We further hypothesize that the intrinsic homogenous linewidth of individual chromophores is most likely narrower than the feature shown in Figure 2.4 and more homogeneous linewidth measurements are discussed in Chapter 4.

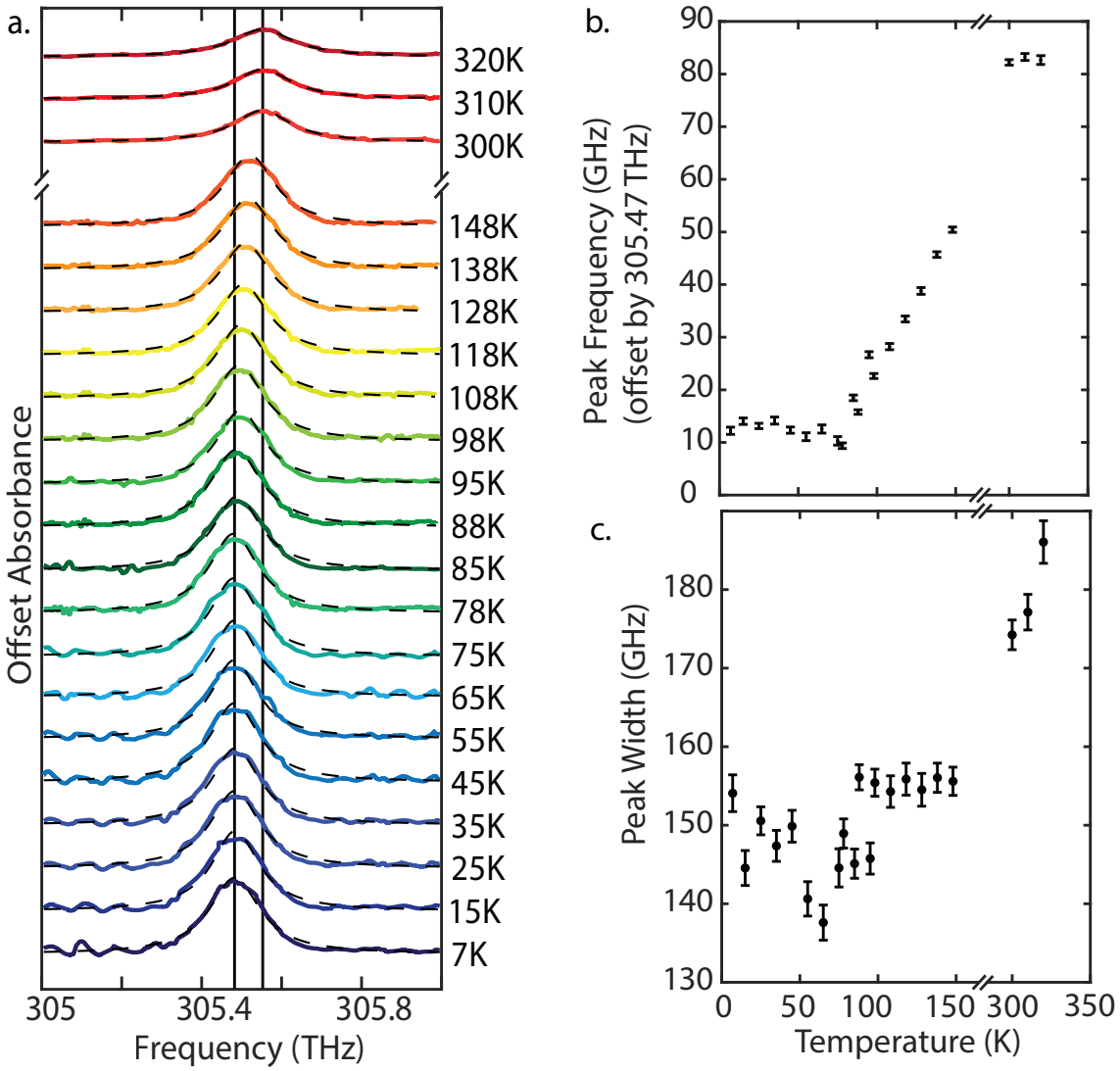

Figure 2.6: Temperature dependent absorption spectrum of (thiolfan)YbCl in 2-MeTHF. a. Absorption spectra of (thiolfan)YbCl in 2-MeTHF from RT to 5 K. The temperature of each spectrum is labeled to the side. Colored lines are original data and dashed lines are Lorentzian fits. b. Absorption peak center frequency vs temperature. The peak center frequency is extracted from Lorentzian fits. c. Absorption FWHM vs temperature. Peak FWHM is also extracted from Lorentzian fits.

2.3 Transition dipole and oscillator strength from absorption spectrum

This 151 GHz ultranarrow transition (IV) (Figure 2.4) comes from the Yb^{3+} inner shell f-f transition ($^2F_{7/2}$ to $^2F_{5/2}$) which is protected by the outer shell electrons (theoretical calculations and experimental support can be found in Section 2.6, 2.5 and Chapter 3).To understand how strong this transition is, we can calculate the oscillator strength of the transition from this narrow absorption spectrum. The calculation follows Ref [38].

The Einstein rate equation is

$$\frac{dN_2}{dt} = -A_{21}N_2 - B_{21}N_2\rho(\omega) + B_{12}N_1\rho(\omega) \tag{2.1}$$

$$\frac{dN_1}{dt} = A_{21}N_2 + B_{21}N_2\rho(\omega) - B_{12}N_1\rho(\omega) \tag{2.2}$$

where N_1 and N_2 are the number of atoms in the lower and upper level. A and B are so called Einstein coefficients. $\rho(\omega) = \rho_0 f(\omega)$ is the energy per volume per unit angular frequency interval. Here $f(\omega)$ is the lineshape function of the laser, $\int f(\omega)d\omega = 1$.

$$B_{21} = \frac{\pi^2 c^3}{\hbar\omega^3}A_{21} \tag{2.3}$$

$$B_{12} = \frac{g_2}{g_1}B_{21} \tag{2.4}$$

g_1 and g_2 are the degeneracy factors of the two levels.
To incorporate the atomic frequency response, we can write

$$b_{12}(\omega) = B_{12}g(\omega) \tag{2.5}$$

where $g(\omega)$ is the spectral lineshape function. $\int g(\omega)d\omega = 1$.

We define the absorption coefficient by

$$i_{out}(\omega) = i_{in}(\omega)e^{-\alpha(\omega)x} \tag{2.6}$$

$$\alpha(\omega) = -\frac{di(\omega)}{i(\omega)dx} \tag{2.7}$$

$i(\omega)$ is the intensity per unit angular frequency interval

$$dI(\omega) = i(\omega)d\omega = c\rho(\omega)d\omega. \tag{2.8}$$

Now we want to relate the absorption coefficient with the Einstein B coefficient. From equation 2.1 we can find laser power change after passing through atoms in volume $A\Delta x$

$$-\Delta P = \hbar\omega A\Delta x(n_1 B_{12} g(\omega)\rho(\omega) - n_2 B_{21} g(\omega)\rho(\omega))d\omega \tag{2.9}$$

$$-\frac{\Delta P}{A\Delta x} = -\frac{di(\omega)}{dx} = \hbar\omega(n_1 B_{12} - n_2 B_{21})g(\omega)\frac{i(\omega)}{c}d\omega. \tag{2.10}$$

So

$$-\frac{di(\omega)}{i(\omega)dx} = \hbar\omega\frac{n_1\frac{g_2}{g_1} - n_2}{c}B_{21}g(\omega). \tag{2.11}$$

This means

$$\alpha(\omega) = \hbar\omega\frac{n_1\frac{g_2}{g_1} - n_2}{c}B_{21}g(\omega). \tag{2.12}$$

Once we calculate the B coefficient from the cross section, we can then calculate the oscillator strength of the transition by

$$f_{12} = \frac{g_2}{g_1}\frac{2\pi\epsilon_0 mc^3}{\omega^2 e^2}A_{21}. \tag{2.13}$$

When doing absorption spectroscopy, we send a beam of light through the sample and measure the output laser power

$$I(\omega) = I_0(\omega)e^{-\alpha(\omega)L}, \tag{2.14}$$

where L is the length of the cuvette. Considering the laser's lineshape $f(\omega)$, we obtain

$$\alpha(\omega) = \int \frac{\hbar\omega' B_{21} g(\omega')}{c}(n_1\frac{g_2}{g_1} - n_2)f(\omega' - \omega)d\omega'. \tag{2.15}$$

Using equation 2.1 we can find when the system reaches equilibrium, the populatons have relationship

$$n_1\frac{g_2}{g_1} - n_2 = \frac{\frac{g_2}{g_1}}{1 + (1 + \frac{g_2}{g_1})\frac{\pi^2 c^3}{\hbar\omega^3}\rho g(\omega)}n \tag{2.16}$$

where $\rho = I/c$. If there is no other broadening and the laser is substantially narrower that the spectrum, we can treat $f(\omega)$ as a delta function and the integral 2.15 will become

$$\alpha(\omega) = \frac{\hbar\omega B_{21} g(\omega)}{c}(n_1 \frac{g_2}{g_1} - n_2) = \frac{\sigma(\omega) n}{1 + 2\frac{\sigma(\omega) I}{\hbar\omega A_{21}}} \tag{2.17}$$

if we assume $g_1 = g_2$. Here $\sigma(\omega)$ is the absorption cross-section defined as

$$\sigma(\omega) = \frac{\pi^2 c^2}{\omega^2} A_{21} g(\omega). \tag{2.18}$$

If we can assume the laser power is weak, $\alpha(\omega)$ and $\sigma(\omega)$ will have the same lineshape as $g(\omega)$

$$\alpha(\omega) = n\sigma(\omega) = n\frac{\pi^2 c^2}{\omega^2} A_{21} g(\omega). \tag{2.19}$$

If we can assume $g(\omega)$ is sharply peaked at ω_0 then after integrating over ω on both side and we will get

$$A_{21} = \frac{1}{n\pi^2 c^2} \int \alpha(\omega)\omega^2 d\omega. \tag{2.20}$$

If there is inhomogeneous broadening and the distribution of molecules with center transition frequency ω is described by the function $h(\omega)$ ($\int h(\omega)d\omega = 1$), then equation should be

$$\alpha(\omega) = \int \frac{\hbar\omega' B_{21} \int g(\omega' - \omega'') h(\omega'')(n_1 \frac{g_2}{g_1} - n_2) d\omega''}{c} f(\omega' - \omega) d\omega'. \tag{2.21}$$

Again if the laser is narrow enough, then

$$\alpha(\omega) = \frac{\hbar\omega B_{21} \int g(\omega - \omega'') h(\omega'')(n_1 \frac{g_2}{g_1} - n_2) d\omega''}{c}, \tag{2.22}$$

where $g(\omega)$ is the spectral lineshape function

$$g(\omega) = \frac{A_{21}}{2\pi} \frac{1}{\omega^2 + (A_{21}/2)^2}. \tag{2.23}$$

If the inhomogeneous broadening is much broader than the life time broadening and laser power is weak, then equation becomes

$$\alpha(\omega) = n\frac{\hbar\omega B_{21} h(\omega)}{c} = n\frac{\pi^2 c^2}{\omega^2} A_{21} h(\omega). \tag{2.24}$$

The lineshape of our absorption spectrum reflects the inhomogeneous broadening. Integrating over ω on both side and we will get

$$A_{21} = \frac{1}{n\pi^2 c^2} \int \alpha(\omega)\omega^2 d\omega, \tag{2.25}$$

which is the same as equation 2.20. With this equation and equation 2.13 we can find

$$f_{12} = \frac{2\epsilon_0 mc}{n\pi\omega^2 e^2} \int \alpha(\omega)\omega^2 d\omega. \tag{2.26}$$

Since we are in solution, we need to correct for the refractive index ($n_{\mathrm{r}} = 1.407$ for THF).

$$\epsilon_0 -> n_{\mathrm{r}}^2 \epsilon_0, \tag{2.27}$$

$$c -> c/n_{\mathrm{r}}. \tag{2.28}$$

What we measured is the transmission spectrum, from which we can get $\alpha(\omega)$

$$\alpha(\omega) = -ln(I_{out}(\omega)/I_{in}(\omega))/L. \tag{2.29}$$

With 4 mM (thiolfan)YbCl in THF in a 1 cm cuvette, we measured the transmission spectrum and calculated the oscillator strength by

$$f_{12} = \frac{2\epsilon_0 mc}{n\pi\omega^2 e^2} \int \alpha(\omega)\omega^2 d\omega = \frac{2\epsilon_0 mc}{n\pi e^2} \int \alpha(\omega) d\omega = \frac{2\epsilon_0 mc}{n\pi e^2} \sum \alpha(\omega)\Delta\omega. \tag{2.30}$$

Assuming it s a two level system and we can treat this transition as an E1 transition, then the transition dipole d_{eg} and saturation intensity I_{sat} can be calculated with

$$d_{\mathrm{eg}} = \sqrt{\frac{3\pi\epsilon_0 \hbar c^3}{\omega^3}\Gamma}, \tag{2.31}$$

$$I_{\mathrm{sat}} = \frac{\hbar\Gamma\omega^3}{12\pi c^2}. \tag{2.32}$$

The following table 2.2 shows the calculated values of oscillator strength, transiton dipole and saturation intensity.

n	4 mM $= 2.4088 \times 10^{24}$ m^{-3}
$\int \sigma(\omega) d\omega$	1.11×10^{-10} m^{2}s^{-1}
f_{12}	9.36×10^{-6}
A_{21}	912 s^{-1}
d_{eg}	1.48×10^{-31} Cm $= 0.044$ D $= 0.017\ ea_0$
I_{sat}	1.43×10^{-4} Wm^{-2}

Table 2.2: Oscillator strength of (thiolfan)YbCl in THF at room temperature

Here is the table that helps to check the units

A_{21}		s^{-1}
B_{21}	$\frac{\pi^2 c^3}{\hbar \omega^3} A_{21}$	$m^3 J^{-1} s^{-2}$
B_{12}	$\frac{g_2}{g_1} B_{21}$	$m^3 J^{-1} s^{-2}$
$\sigma(\omega)$	$\frac{\hbar \omega B_{12} g(\omega)}{c}$	m^2
$\alpha(\omega)$	$\frac{\hbar \omega B_{12} g(\omega)}{c} n$	m^{-1}
f_{12}	$\frac{g_2}{g_1} \frac{2\pi \epsilon_0 m c^3}{\omega^2 e^2} A_{21}$	1

Table 2.3: Helper table for unit check of the oscillator strength calculation

We find that the measured oscillator strength of this transition (IV) is 9.36×10^{-6} which is on the order of $10^{-6} - 10^{-5}$. This is strong comparing to the oscillator strength of M1 transitions and it is close to some E1 transitions[39]. Although the $^2F_{7/2}$ to $^2F_{5/2}$ transition of a gas phase Yb^{3+} is E1 forbidden, it is stronger in our liquid molecular system with a Yb^{3+} metal center. This indicates that the surrounding ligands mix the states so that this transition is open but it only mixes a little so that this transition is still atomic like and the linewidth is still narrow. In fact, it is the narrowest we find for a room temperature solution. In Section 2.6 we will discuss more about theoretical calculations of electronic structure and oscillator strength of this molecule.

2.4 Zeeman splitting at room temperature

This 151 GHz is so narrow that makes it possible to resolve some magnetic field splittings (Zeeman splittings) of this room temperature liquid system, which it typically not practical with broadband absorbing solutions. We performed magnetic circular dichroism (MCD) measurements which measure the differential absorption of σ^+ and σ^- circularly polarized light induced in a sample under a strong magnetic field. Typically, resolving these shifts requires a superconducting magnet, cryogenic temperatures, and lock-in detection[40]. In contrast, we easily measured these shifts using a permanent rare-earth magnet set under the sample at room temperature (Figure 2.2). With the presence of an external magnetic field $B = 0.38$ T, we were able to detect a 23 GHz splitting in the absorption spectrum between σ^+ and σ^- light (Figure 2.7). The sample we used was 3 mM (thiolfan)YbCl(THF) in a 1cm cuvette.

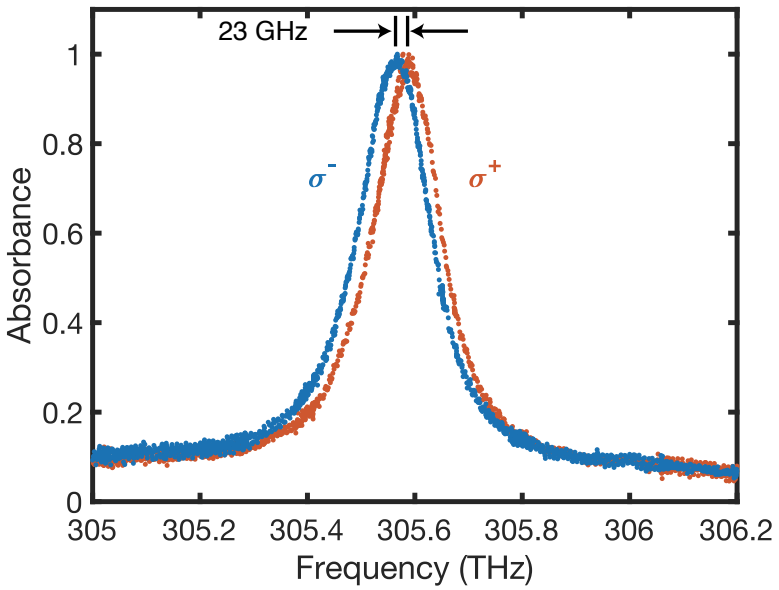

Figure 2.7: Room temperature Zeeman splitting under a static magnetic field of 0.38T. Absorption is measured at room temperature with both σ^+ and σ^- light. The splitting is 23 GHz and the full width at half maximum of the transition is 151 GHz.

This splitting corresponds to an effective transition magnetic moment of 2.2 $\pm$ 0.1 μ_{B} and the effective g factor is $g_{\mathrm{eff}} = 2.2 \pm 0.1$. It is calculated with

$$\Delta E = h\Delta f = 2\mu_{\mathrm{eff}} B = 2g_{\mathrm{eff}}\mu_{\mathrm{B}} B \tag{2.33}$$

where Δf is the splitting, B is the applied external magnetic field and μ_{B} is Bohr magneton.

We then measured the absorption spectrum of σ^+ and σ^- light under various static magnetic field ranging from 0 to 0.38 T. Spectra were fitted with Lorentzian function, and center of each absorption peak was extracted from the fits. Then we got the splittings from the peak maximum difference between σ^+ and σ^- absorption spectra. We find that the splittings grow linearly with the external magnetic field as shown in Figure 2.8 a. The absorption difference is shown in Figure 2.8 b. This error-signal-like feature is generated from a direct subtraction between the absorption of σ^+ and σ^- light and it can be viewed as the first-order derivative of the original absorption lineshape.

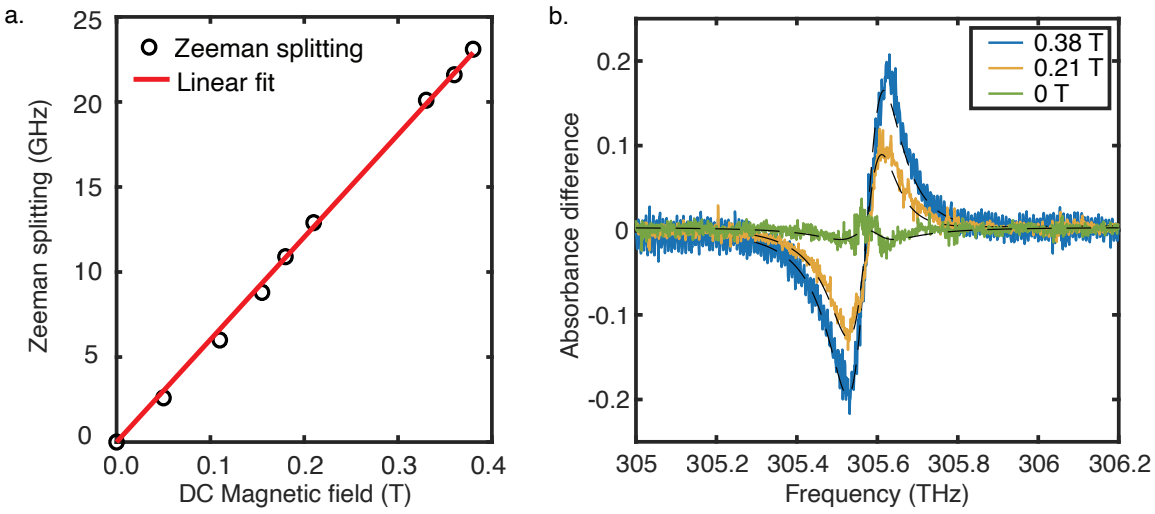

Figure 2.8: Room temperature Zeeman splitting vs static magnetic field strength. a. Linear relationship between Zeeman splittings and applied external magnetic field strength. b. Differential absorbance of σ^+ and σ^- light under varying static magnetic field strengths. Black dashed lines are the fits.

An interesting demonstration of the application of this error signal is laser locking. The idea is to measure the absorption difference of σ^+ and σ^- light and correct laser driftings based on the sign and magnitude of this difference. The setup is shown in Figure 2.9. The incident light is an even combination of σ^+ and σ^- light which is vertically polarized. Then it is absorbed by the sample and the absorption depends on the frequency and polarization. The quarter waveplate and polarization beam splitter separate the σ^+ and σ^- light to two paths for intensity detection and error signal is the intensity difference. This is called Dichroic Absorptive LIquid clock (DALI). Without adding a feedback loop, I was able to manually lock the Ti:Sapphire laser according to the error signal. Without locking, the laser drifted 5 MHz in a hour whereas with locking, it only fluctuated 1 MHz in 25 min.

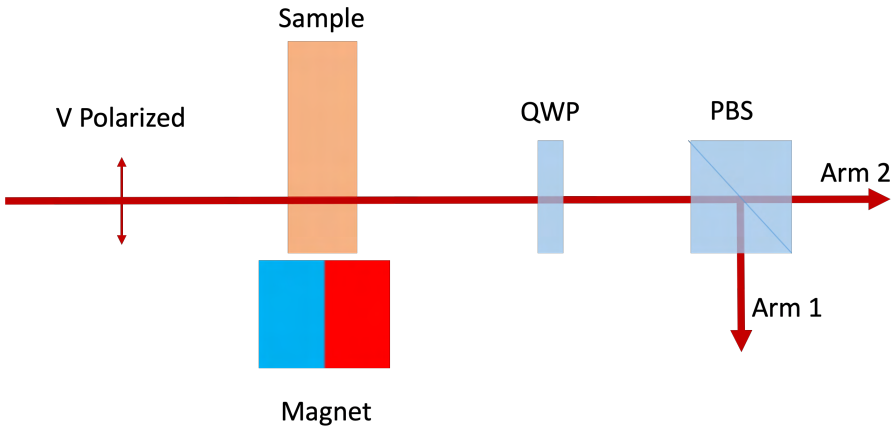

Figure 2.9: Dichroic Absorptive LIquid clock (DALI).

2.5 Electron paramagnetic resonance (EPR) spectrum

To further understand the properties of the ground state doublet, continuous-wave (CW) EPR and pulsed EPR measurements were done and analyzed by Dr. Paul H. Oyala in Caltech and sample were prepared by Yi Shen. CW X-band (9.6 GHz) EPR spectra were acquired using a Bruker EMX CW-EPR spectrometer equipped with an ER- 4116DM Dual Mode resonator operating in perpendicular mode. Pulse EPR data were acquired using a

Bruker ELEXSYS E-580 pulse EPR spectrometer operating at X-band with a microwave frequency of 9.36 GHz using a MS-5 split ring resonator. More details of EPR results are available in Ref [28]. Here we only show some main findings.

CW-EPR spectra of (thiolfan)YbCl were first measured in 2-MeTHF as a frozen glass, which exhibit very prominent, narrow positive features centered around a peak at 92.6 mT (Figure 2.10). Since in a glass molecules are randomly oriented, this dominant narrow feature suggests that in the inhomogeneously broadened environment, a certain orientation is slightly more dominant and is picked up by CW-EPR measurement. The other small side features are from $^{171}Yb^{3+}$ and $^{173}Yb^{3+}$ who has non-zero nuclear spins.

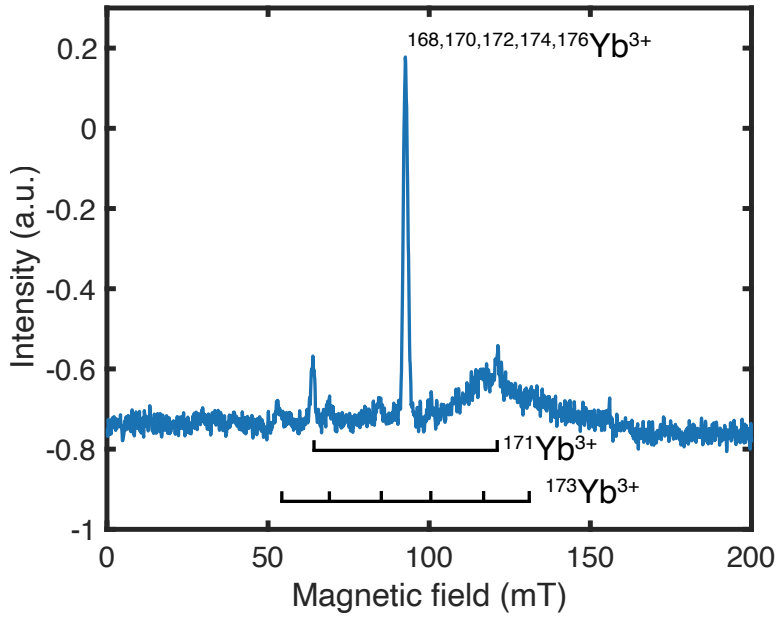

Figure 2.10: CW-EPR spectrum of (thiolfan)YbCl in 2-MeTHF at 5 K. The main peak is from Yb isotopes with zero nuclei spins (69.68% abundance) and side peaks are from $^{171}Yb^{3+}$ (I = 1/2, 16.10% abundance) and $^{173}Yb^{3+}$ (I = 5/2, 14.22% abundance).

EPR addresses the ground states and the g-factor is calculated by

$$\Delta E = h\nu = 2g_{\mathrm{g}}\mu_{\mathrm{B}}B \tag{2.34}$$

where ΔE is the energy splitting, h is Planck's constant, ν is resonance frequency, μ_{B} is Bohr magneton and B is magnetic field. With the X-band EPR we have $\nu = 9.6$ GHz and $B = 92.6$ mT, which leads to $g_{\mathrm{g}} = 3.718 \pm 0.004$.

In order to evaluate temporal information of the Zeeman splittings, pulse EPR spectroscopy (field swept electron spin echo (ESE) EPR) was done. In contrast with the 1.6 mT narrow peak in CW-EPR, ESE-EPR exhibits extremely broad linewidths, with intensity starting near 140 mT and continuing up to the high-field limit of our electromagnet at 1478.5 mT. This indicates that the majority of molecular orientations exhibit significant inhomogeneous broadening in the field ranges accessible, and that there is significant spectral intensity above the field ranges accessible by our instrumentation. Spin relaxation measurements via pulse EPR were performed (table 2.4). In general, at temperatures where the spin-lattice relaxation time (T_1) is much longer than the phase memory time (T_{m}), EPR spectra typically exhibit Lorentzian lineshapes with approximate homogeneous peak-peak linewidths proportional to $\frac{2}{\sqrt{3}T_{\mathrm{m}}}$. The shortest T_{m} value we measure is 0.82 μs at 320 mT, which would correspond to a linewidth of approximately 2 mT – this is in reasonable agreement with the peak-peak linewidth of the sharp transitions resolved at g = 3.718 in the CW-EPR spectrum (1.6 mT) which correspond to a very small subset of molecular orientations around the measurement direction, but it is two orders of magnitude smaller than the observed linewidths at higher fields in the field-swept pulse EPR spectrum. Therefore, the extremely broad linewidths must be due to inhomogeneous broadening, which most likely arises from heterogeneity in g values of the spin system due to slight variations in spin orbit coupling contributions.

	3.6 K		5.8 K	
	320 mT	1200 mT	320 mT	1200 mT
T_1	518 μs	116 μs	23.5 μs	10.4 μs
T_m	0.82 μs	1.09 μs		

Table 2.4: Spin-lattice relaxation time (T_1) and phase memory time (T_m). T_1 is measured with inversion recovery and T_m is measured with Hahn Echo decay.

2.6 Theoretical calculations

To study why this absorption spectrum is narrow and get a better understanding on the composition of the ground and excited states of this ultranarrow transition, electronic structure of the molecule was calculated by Claire Dickerson from Anastassia N. Alexandrova group in UCLA. Here we will show some main results.

The isolated Yb^{3+} ion possesses seven degenerate states arising from orbitals of the 4f shell with 13 valence electrons ($4f^{13}$). Large electronic spin-orbit coupling separates the $4f$ states into spin-orbit states, creating the primary optical (near infrared)NIR transition from the 8-state $^2F_{7/2}$ to the 6-state $^2F_{5/2}$ manifolds[25]. In a molecular framework, each spin-orbit manifold is further split due to the ligand-field contributions, giving rise to the individual electronic transitions II-IV (Figure 2.3). Electronic structure and oscillator strength are calculated with multireference theory (more details in Ref [28]).

2.6.1 Electronic structure and oscillator strength

Figure 2.11 shows the calculated spin-orbit and ligand field splittings of the ground and excited states of (thiolfan)YbCl(THF). As evident in the small spread of transitions II-IV (2.3), lanthanide complexes possess strong spin-orbit coupling (250 THz) and much smaller ligand field splitting (2 - 30 THz) than typical transition metal complexes[41][42]. The

ligand field splits the spin-orbit states into four and three Kramers doublets. Our ultranarrow transition IV is from state (1,2) to state (9,10), which is primarily composed of $4f$ atomic states. A visual guide, shown in Figure 2.12, captures the primary states that contribute to the ground and excited state wavefunctions, although we note that these pictures do not reflect the overall multireference nature of the molecular orbitals.

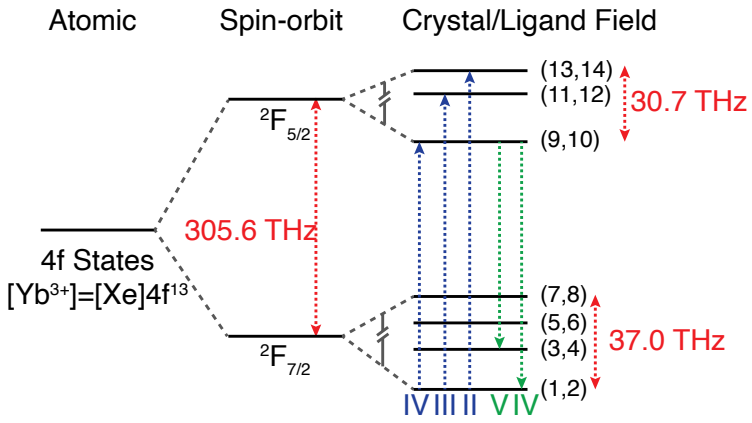

Figure 2.11: Electronic structure diagram. It shows the incorporation of spin-orbit and ligand field effects on the Yb^{3+} atomic orbitals, calculated with CASSCF/CASPT2/RASSI-SOC level of theory.

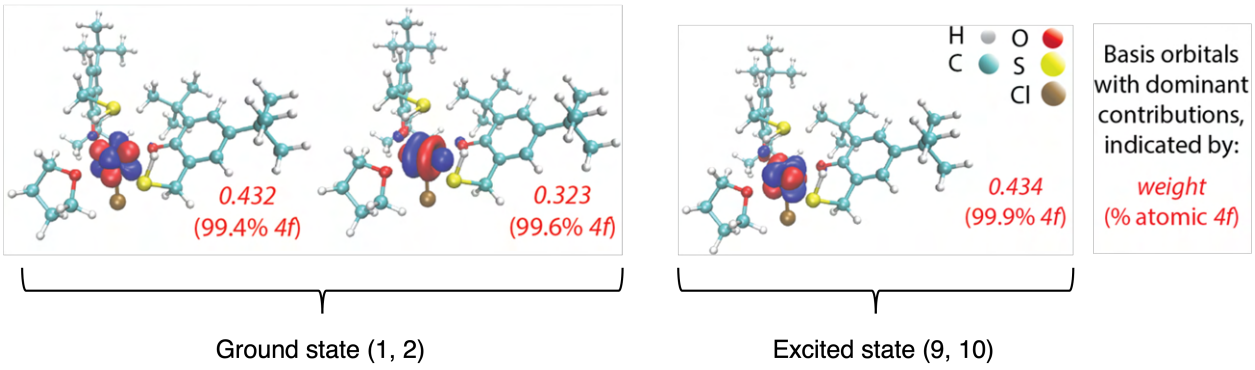

Figure 2.12: Visualization of the CASSCF basis orbitals that have dominant contribution(s) to the molecular orbitals involved with transition IV, demonstrating the "atom-like" properties.

The theoretically calculated transition energies and oscillator strength, as well as experimental data are shown in Figure 2.13. In this Figure, absorption is measured with UV-Vis spectrometer and emission is collected in an all-reflective off-axis parabolic epifluorescence setup, after which it goes through a Mach-Zender interferometer and towards superconducting nanowire single photon detectors[43]. These experiments were done by Ashley with the help of Timothy L. Atallah.

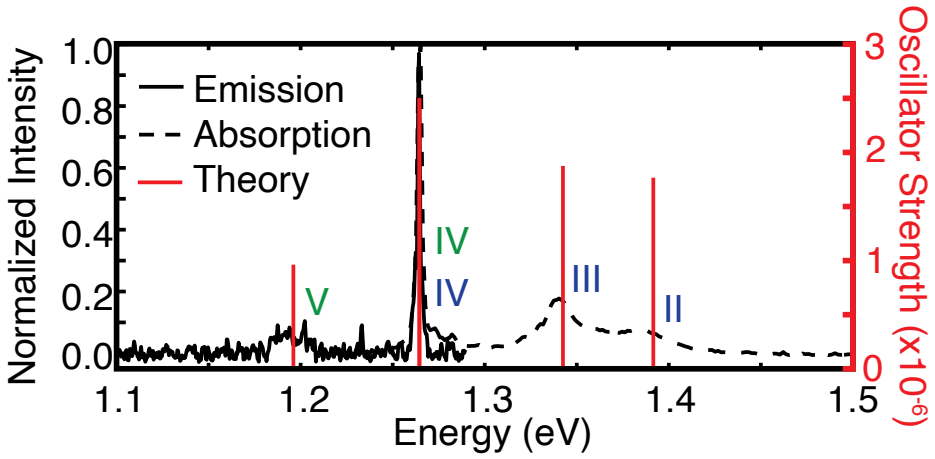

Figure 2.13: Comparison between emission/absorption data and the transition energies and oscillator strength calculated by multireference calculations. Sample used is (thiolfan)YbCl(THF).

Notice here the calculated oscillator strength is to the same magnitude as measured value (9.36×10^{-6}), which is way stronger than a pure M1 transition but close to the oscillator strength of E1 transitions. E1 interaction can be written as

$$H_{\mathrm{E1}} = -\boldsymbol{d} \cdot \boldsymbol{E} \tag{2.35}$$

with electric dipole moment $\boldsymbol{d} = -e\boldsymbol{r}$. $\boldsymbol{E}$ is the electric field. Electric dipole oscillator strengths then can be written as

$$E1_{\mathrm{f}\leftarrow\mathrm{i}} = \frac{2m_{\mathrm{e}}(E_{\mathrm{f}} - E_{\mathrm{i}})}{3\hbar^2 e^2} |\langle f| e\boldsymbol{r} |i\rangle|^2. \tag{2.36}$$

M1 interaction can be written as

$$H_{\mathrm{M1}} = -\boldsymbol{\mu} \cdot \boldsymbol{B} \tag{2.37}$$

with magnetic dipole moment $\boldsymbol{\mu}$ and magnetic field $\boldsymbol{B}$. Magnetic dipole oscillator strength then can be written as

$$M1_{\mathrm{f}\leftarrow\mathrm{i}} = \frac{2m_{\mathrm{e}}(E_{\mathrm{f}} - E_{\mathrm{i}})}{3\hbar^2 e^2 c^2} |\langle f| \boldsymbol{\mu} |i\rangle|^2. \tag{2.38}$$

The atomic $^2\mathrm{F}_{7/2}$ to $^2\mathrm{F}_{5/2}$ transition is E1 forbidden. Barry Li from Justin Caram group in UCLA calculated the M1 oscillator strength from an atomic model and got 10^{-11} to 10^{-8} (SI of [28]). In our molecular system, we find that inclusion of the virtual Yb 5d orbitals into the '13 electrons in 12 orbitals' active space (i.e., $7 \times \mathrm{Yb}(4f) + 5 \times \mathrm{Yb}(5d)$) is critical for obtaining the transition energies and oscillator strengths because they show small ligand mixing. The coupling of $5d$ and ligands brings down the energies of $5d$ orbitals, making them available for coupling with $4f$ orbitals. The $4f/5d$ and $5d$/ligand mixing, especially mixing with $5d$, attribute to the enhanced oscillator strength. Notice here in gas phase where molecules can rotate freely, together with rotations and vibrations, the eigenstates of energy should also be eigenstates of parity, meaning each eigenstate should either be parity even or odd. The free transition should either be E1 allowed or forbidden. However in liquid phase, collisions and environmental fluctuations will make the eigenstates of energy be a superposition of those parity eigenstates in gas phase, leading to a stronger oscillator strength. The good match between theoretical calculations and experimental transition energies illustrates the role of spin-orbit coupling and asymmetric ligand field in enhancing absorption and points toward molecular design principles that creates well-protected yet observable electronic transitions in lanthanide complexes.

2.6.2 Landé g-factor

We got an effective transition magnetic moment of 2.2 ± 0.1 μ_{B} with effective g-factor g_{eff} = 2.2 ± 0.1 from he room temperature Zeeman splittings we measured (Figure 2.7). This describes the magnetic property of ground and excited states. From the EPR spectrum

(Figure 2.10), we got the ground state g-factor $g_{\mathrm{g}} = 3.718 \pm 0.004$. This describes the magnetic property of ground states. With this two we can do subtraction to find the excited state g-factor

$$\begin{aligned} \Delta E_{\mathrm{g}} &= 2g_{\mathrm{g}}\mu_{\mathrm{B}}B \\ \Delta E_{\mathrm{e}} &= 2g_{\mathrm{e}}\mu_{\mathrm{B}}B \\ E_{\sigma^+} - E_{\sigma^-} &= \Delta E_{\mathrm{g}} - \Delta E_{\mathrm{e}} = 2(g_{\mathrm{g}} - g_{\mathrm{e}})\mu_{\mathrm{B}}B = 2g_{\mathrm{eff}}\mu_{\mathrm{B}}B \\ g_{\mathrm{e}} &= g_{\mathrm{g}} - g_{\mathrm{eff}}. \end{aligned} \tag{2.39}$$

We got $g_{\mathrm{e}} = 1.6 \pm 0.1$. For comparison, we can calculate the g-factors for a gas phase Yb^{3+} ion with

$$g_{\mathrm{J}} = g_{\mathrm{L}}\frac{J(J+1) + L(L+1) - S(S+1)}{2J(J+1)} + g_{\mathrm{S}}\frac{J(J+1) - L(L+1) + S(S+1)}{2J(J+1)} \tag{2.40}$$

where the the orbital g_{L} is equal to 1, and under the approximation $g_{\mathrm{S}} = 2$, the above expression simplifies to

$$g_{\mathrm{J}} = 1 + \frac{J(J+1) - L(L+1) + S(S+1)}{2J(J+1)} \tag{2.41}$$

and under weak field, the Zeeman shift is

$$\Delta E = g_{\mathrm{J}} m_{\mathrm{j}} \mu_{\mathrm{B}} B. \tag{2.42}$$

For the ground states ${}^2\mathrm{F}_{7/2}, m_{\mathrm{j}} = \pm 7/2$, $|g_{\mathrm{J}} m_{\mathrm{j}}| = 4$ and for the excited states ${}^2\mathrm{F}_{5/2}, m_{\mathrm{j}} = \pm 5/2$, $|g_{\mathrm{J}} m_{\mathrm{j}}| = 2.143$. We notice here these numbers are close to the values we got from experiments, which suggests that our ultranarrow transition is from ground states that are similar to atomic ${}^2\mathrm{F}_{7/2}, m_{\mathrm{j}} = \pm 7/2$ to excited states that are similar to atomic ${}^2\mathrm{F}_{5/2}, m_{\mathrm{j}} = \pm 5/2$. Figure 2.14 is a schematic drawing of ligand field splittings and Zeeman splittings. Note here we use atomic notations to label these states because they are atomic-like. But indeed these are all molecular states with $5d$ and ligand mixings.

Our high-level RASSI-SOC calculations produces g-tensor as shown in the table 2.5. Again the numbers are close to values we measured from EPR and room temperature Zeeman

spectra. Also need to notice here the calculated g-tensor is super anisotropic, which makes it a good candidate to present single molecule magnet behavior[44].

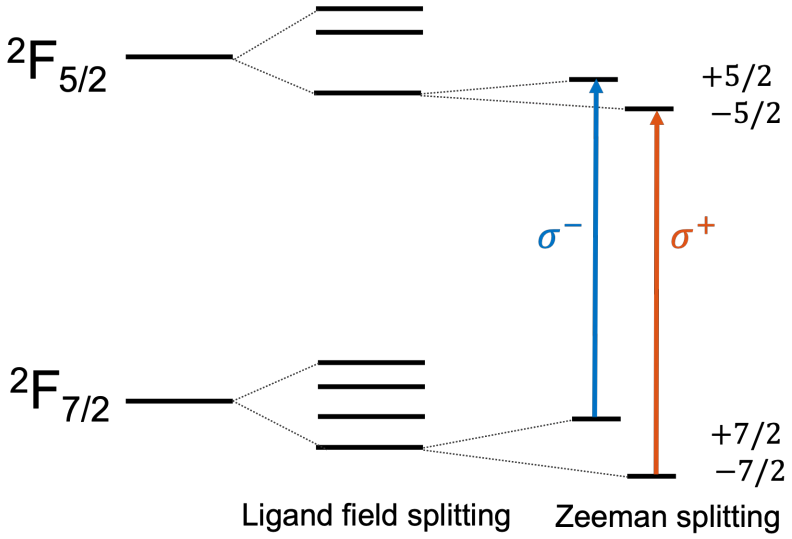

Figure 2.14: Schematic drawing of electronic structure and Zeeman levels of the Yb^{3+} center in (thiolfan)YbCl(THF).

	Ground states	Excited states
EPR	3.718 ± 0.004	
Derived from EPR and RT Zeeman effect		2.2 ± 0.1
Calculated from RASSI-SOC	$g_x = 3.75$ $g_y = 0.17$ $g_y = 0.19$	$g_x = 2.14$ $g_z = 0.09$ $g_z = 0.08$
Gas Phase Yb^{3+}	4	2.14

Table 2.5: Comparison of measured and calculated g-factors for the ground and excited states of transition IV in (thiolfan)YbCl(THF), both lower than the theoretical gas phase limits.

CHAPTER 3

Magnetic field sensing

As discussed in Section 2.4, this atomic-like transition is so narrow that we are able to direct resolve Zeeman splitings at room temperature. The extraordinarily narrow linewidth, relatively strong oscillator strength and effective g-factor make the system possible for magnetic field sensing. Here we demonstrate our efforts on DC and AC magnetic field sensing and imaging using this ultranarrow linewidth. We are able to achieve sensitivity on the scale of Earth's magnetic field.

3.1 Experimental setup

We employed a home-made external cavity diode laser (ECDL) for magnetic field imaging, as shown in Figure 3.1. The laser was tuned to the half maximum of the absorption peak of the sample. We used two lenses to expand the laser beam size, which enabled us to cover the entire cuvette. A permanent magnet (N52 grade magnet from Magneto Inc) was mounted onto a rotating motor (uxcell DC 24V motor) beneath the sample. The sample we used was $\sim$3 mM (thiolfan)YbCl(THF) in a 1 cm cuvette. The transmitted beam was captured using a webcam, and the pixel value was converted to magnetic field strength using calibration measurements obtained using a gaussmeter (Lakeshore 410) at specific distances from the permanent magnet.

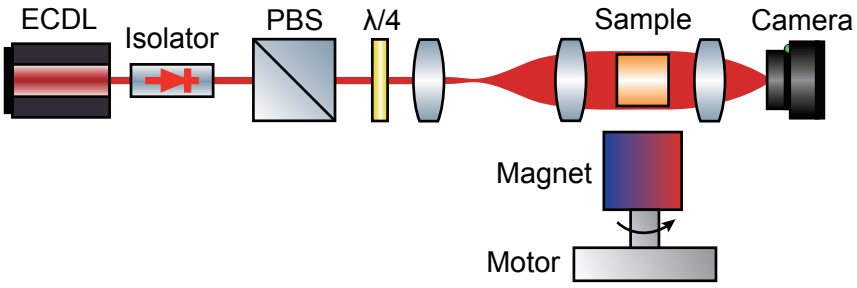

Figure 3.1: Optical setup for magnetic field imaging.

Figure 3.2 shows the optical setup for DC magnetic field sensing. A M Squared SolsTis Ti:Sapph laser with a Lighthouse Sproud pump laser system was used to generate 304 THz to 307 THz light. The laser power required for this measurement was under 30 mW. The beam was split into two paths, each passing through an acousto-optic modulator (AOM, Gooch & Housego 2308-1-1.06 and Isomet SR48607) set at f and $f + \Delta f$ respectively, before being combined at another polarizing beam splitter. The resulting beam was oscillating between right and left-hand circular polarizations at $\Delta f = 100$ kHz. The amplitude of the transmitted light was detected with a photodetector (Thorlabs PDA8A) and the amplitude of the 100 kHz signal was analyzed using a spectrum analyzer (Agilent Technologies N9010A).

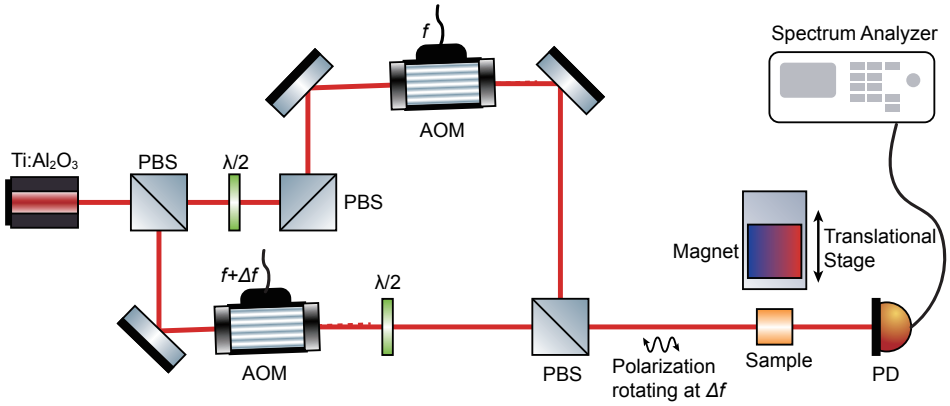

Figure 3.2: Optical setup for DC magnetic field measurement with polarization modulated beam.

Figure 3.3 shows the optical setup for AC magnetic field sensing. To measure an AC field, we used the same setup as in Figure 3.2, but added a Helmholtz coil around the sample holder. This produced two additional sidebands at frequency $\Delta f \pm f_{AC}$, and their amplitude was monitored by a spectrum analyzer (Agilent Technologies N9010A). The AC magnetic field was generated using an arbitrary waveform generator (Agilent 33220A) which supplies an oscillating current to the coils (100 turns with a diameter of 3 cm). The field was then measured by a gaussmeter (Lakeshore 410) to confirm its magnitude.

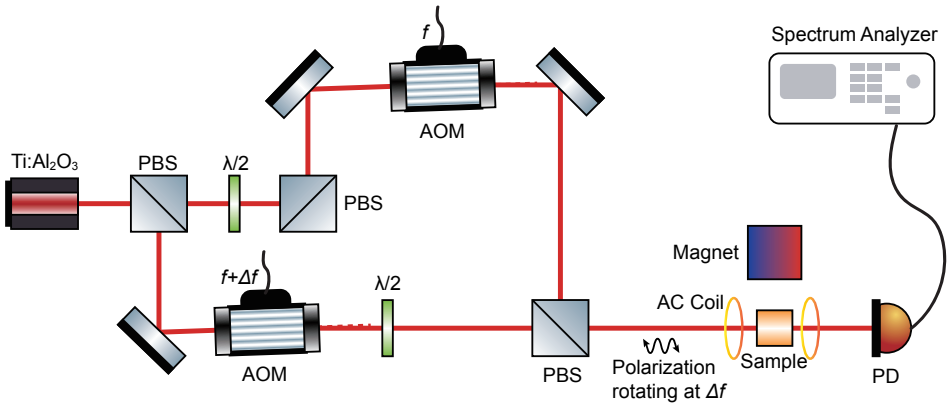

Figure 3.3: Optical setup for AC magnetic field measurement with polarization modulated beam.

3.2 Magnetic field imaging

The transmission intensity of a circularly polarized light at resonant frequency depends on the strength of the external field along the laser propagation direction. This is because absorption spectra of circularly polarized light shifts under varying DC magnetic fields (Figure 2.7, 2.8). For example, if our laser is tuned to around 305.65 THz (to the higher frequency side of the center resonance) and is σ^+ polarized relative to the magnetic field, stronger magnetic field will shift the σ^+ absorption to higher frequency such that our laser is closer to the center resonance. This means the laser is absorbed more and the transmitted intensity measured

will be weaker. Similarly weaker field leads to a weaker absorption and stronger transmission. So the pixel value can reflect the strength of the imaged magnetic field. The setup is shown in Figure 3.1. As we rotate the magnet, the magnetic field strength along the laser direction will be oscillating. Thus the transmitted laser intensity will oscillating accordingly. Or in other words, the image will blink. Video showing the change in intensity of the transmission image can be found in the extra SI material of Ref [28]. Figure 3.4 shows two snapshots from the video. We can see that the transmission intensity increases as it gets closer to the magnet, which indicates a larger Zeeman splitting and stronger magnetic field. The pixel intensity matches the measured magnetic field strength. In this way we can visualize the magnetic field generated by the permanent magnet below the sample cuvette. The sensitivity of this measurement depends on the uncertainty of the g-factor and the resolution of the absorption measurement, leading to a sensitivity of 0.05 T (500 G) with this MCD setup.

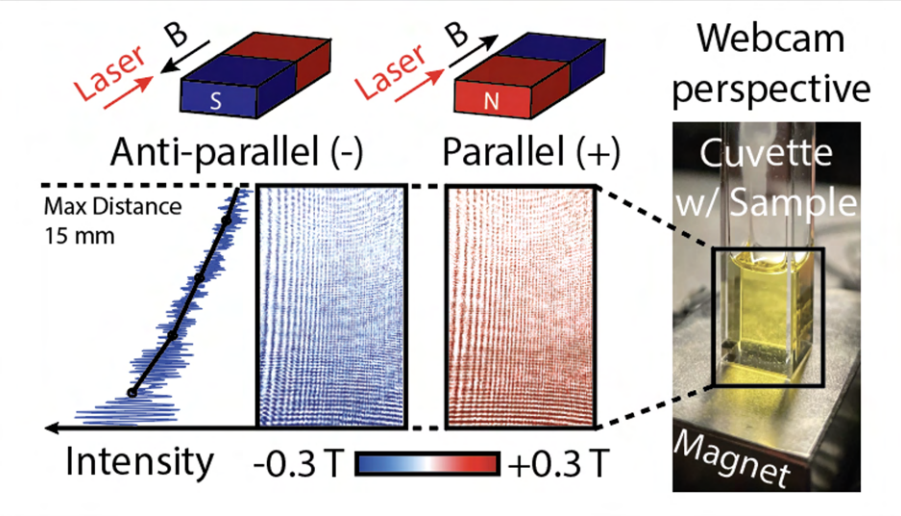

Figure 3.4: MCD imaging snapshots. Right is a picture of the sample on top of a permanent magnet. Left shows two snapshots of dynamic MCD imaging video demonstrating parallel and anti-parallel orientations of the magnetic field and laser propagation. The pixel intensity and magnetic field strength measured by gaussmeter measurements at multiple distances away from the magnet are shown on the left plot (x-axis: pixel intensity, y-axis: distance from magnet, blue: pixel intensity, black: gaussmeter measurements).

3.3 DC magnetic field sensing

With the linear relationship between Zeeman splitting and applied magnetic field (Figure 2.8 a), it is straight froward to implement our liquid sample to be a DC magnetic field sensor. For instance, we can measure the absorption spectrum with σ^+ light and σ^- light, then extract magnetic field strength from the measured splitting knowing the value of effective g-factor. However this requires two full scan of the whole absorption spectrum, which is actually not necessary. A better way to do this is to fix laser frequency but modulate laser polarization. If we tune our laser's frequency to where the absorption is at half maximum (as shown in Figure 3.5 a), the sample will absorb quite differently between σ^+ and σ^- polarized light and that difference is proportional to the strength of the applied external magnetic field. When polarization of the incident light is oscillating between σ^+ and σ^- at frequency f_{pol}, the transmission intensity will oscillate at the same frequency, with amplitude that is proportional to the applied magnetic field strength.

To generate a laser beam with polarization oscillating between right and left-hand polarization at f_{pol}, we first split the laser into two AOMs. One diffract the beam with frequency f_{a} and the other diffract the beam with frequency f_{b}. Beam a is vertically polarized

$$\boldsymbol{E}_{\mathrm{a}} = E_0 e^{i(\boldsymbol{k}_{\mathrm{a}} z - \omega_{\mathrm{a}} t)} \hat{\boldsymbol{y}}. \tag{3.1}$$

Beam b is horizontally polarized

$$\boldsymbol{E}_{\mathrm{b}} = E_0 e^{i(\boldsymbol{k}_{\mathrm{b}} z - \omega_{\mathrm{b}} t)} \hat{\boldsymbol{x}}. \tag{3.2}$$

Then we combine them with a PBS, at the sample the electric field will be

$$\begin{aligned} \boldsymbol{E} &= E_0 e^{-i\omega_{\mathrm{a}} t} \hat{\boldsymbol{y}} + E_0 e^{-i\omega_{\mathrm{b}} t + i\phi} \hat{\boldsymbol{x}} \\ &= E_0 e^{-i\omega_{\mathrm{a}} t} (e^{-i\Delta\omega t + i\phi} \hat{\boldsymbol{x}} + \hat{\boldsymbol{y}}) \end{aligned} \tag{3.3}$$

where $\Delta\omega = \omega_{\mathrm{b}} - \omega_{\mathrm{a}}$. The term $e^{-i\Delta\omega t + i\phi} \hat{\boldsymbol{x}} + \hat{\boldsymbol{y}}$ shows the polarization of the field and it is oscillating at frequency $f_{\mathrm{pol}} = \Delta f = \frac{\Delta\omega}{2\pi} = f_{\mathrm{b}} - f_{\mathrm{a}}$.

We set the two AOMs at a frequency difference of 100 kHz, which produced a beam whose polarization was oscillating at frequency $f_{\text{pol}} = 100$ kHz. We then examined how the amplitude of the transmitted light changes with the static magnetic field (Figure 3.5 b). We used around 3 mM (thiolfan)YbCl(THF) in a 1 cm cuvette. We observed the expected linear trend, confirming the capability of this sample to measure static magnetic fields down to a 0.025 T (250 G) difference.

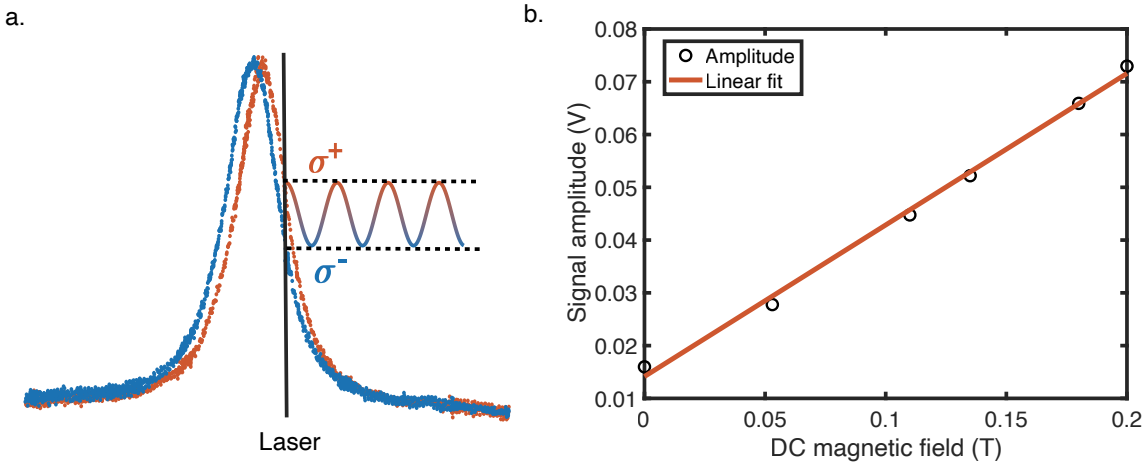

Figure 3.5: DC magnetic field sensing with polarization modulated beam. a. Schematic drawing explaining how the transmission intensity oscillating with polarization. b. Amplitude of the oscillating transmitted light intensity measured with static magnetic field (0 - 0.2 T).

3.4 AC magnetic field sensing

We used the same method we discussed in the previous section to measure AC magnetic field. On top of the non-zero external magnetic field B_0, we added an AC magnetic field with strength B_1 and frequency f_{B_1}. Since the amplitude of the oscillating transmission intensity reflects strength of magnetic field, the transmission will be amplitude modulated

at frequency f_{B_1} with the AC magnetic field. And the depth of this amplitude modulation should be proportional to B_1. For example, under a static magnetic, the transmission signal I_t measured with laser polarization being modulated at f_{pol} will be

$$I_t = kB_0\cos(2\pi f_{pol}t) \tag{3.4}$$

where k is a factor denoting the linear relationship between applied magnetic field and signal amplitude. When we add an extra AC magnetic field $B_1\cos(2\pi f_{B_1}t)$, the signal will be

$$\begin{aligned} I_t &= k(B_0 + B_1\cos(2\pi f_{B_1}t))\cos(2\pi f_{pol}t) \\ &= kB_0\cos(2\pi f_{pol}t) + \frac{1}{2}kB_1\cos(2\pi(f_{pol}+f_{B_1})t) + \frac{1}{2}kB_1\cos(2\pi(f_{pol}-f_{B_1})t). \end{aligned} \tag{3.5}$$

So in the frequency domain, there will be two sidebands at frequency $f_{pol}+f_{B_1}$ and $f_{pol}-f_{B_1}$, whose amplitude $\frac{1}{2}kB_1$ is proportional to the amplitude of the AC magnetic field B_1.

We used a pair of Helmholtz coil to produce AC magnetic field (Figure 3.6 a). Each coil was 100 turns with diameters around 3 cm, driven with function generator to generate AC magnetic field at the sample. The field on axis of a current loop can be calculated with

$$B_z = \frac{\mu_0}{4\pi}\frac{2\pi R^2 I}{(z^2+R^2)^{3/2}} \tag{3.6}$$

where B_z is the magnetic field along the axis, μ_0 is vacuum permeability, R is radius of the current loop, I is current and z is distance from the loop center. With 0.15 mA current, at 1 cm away from the coil center, the magnetic field is around 3.6 Gs and this is confirmed with a gaussmeter.

The amplitude modulated signal was observed with a spectrum analyzer. Notice that the spectrum analyzer is showing power spectrum which is the square of the amplitude $\frac{1}{2}kB_1$. Three peaks showed up on the spectrum analyzer – one at frequency f_{pol} and two side peaks f_{B_1} away from it. The sideband peak heights increase with the amplitude of the applied AC magnetic field. The (thiolfan)YbCl(THF) solution shows a monotonically increasing linear trend with the AC magnetic field, whereas the THF solvent and air show no dependence on the magnetic field (Figure 3.6 b). With this method, we measured AC magnetic fields at

1 kHz down to 0.5 G, which is the scale of the Earth's magnetic field. Even though these measurements are performed with a room temperature solution, we can achieve a sensitivity of $\mu\mathrm{T}/\sqrt{\mathrm{Hz}}$ scale.

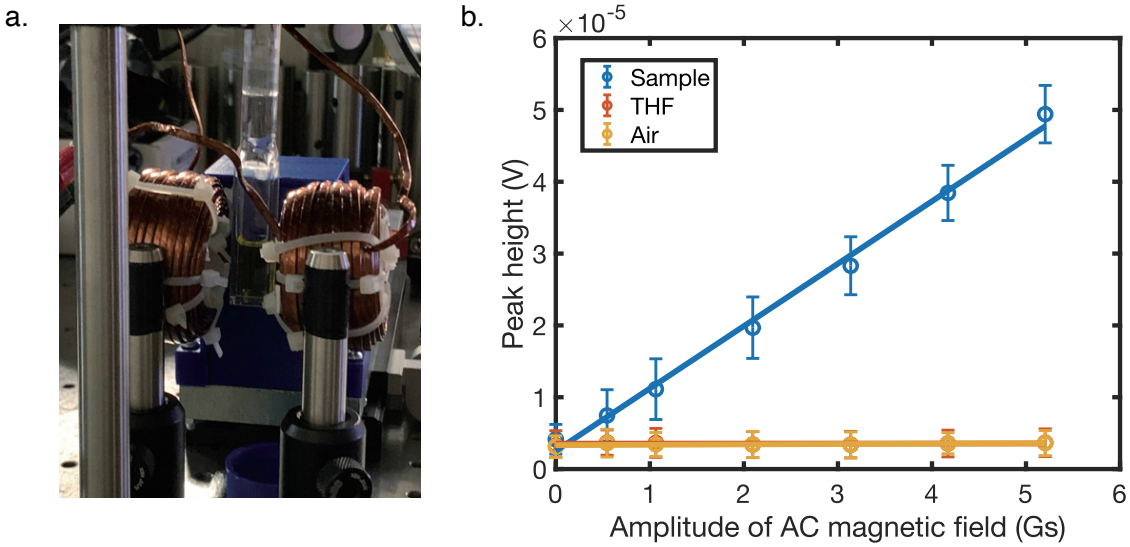

Figure 3.6: AC magnetic field sensing with polarization modulated beam. a. Picture of the Helmholtz coil sandwiching the liquid sample ((thiolfan)YbCl in THF). b. Increase of frequency modulation signal with the amplitude of the applied AC magnetic field in the presence of (thiolfan)YbCl(THF). Measurements were done with resolution bandwidth of 3 Hz. Considering measurement duration and sampling frequency, the noise level of a single measurement was around 2.4 $\times 10^{-6}$ V which corresponds to 28 μT.

3.5 Sensitivity comparison

There are several important figures of merit in comparing ALMS to other magnetic field sensing technologies – sensitivity, frequency range, and distance from sample. The most important figure of merit is magnetic field sensitivity, which describes the smallest magnetic field that can be detected within a given measurement time. For (thiolfan)YbCl(THF), the

sensitivity is governed by the absorption change upon applying a magnetic field, where the most drastic response comes with the steep slopes in the absorption feature. We estimate that our limit in sensitivity is set by the signal-to-noise difference in transmission, where our best resolution comes from the measurement of a small AC magnetic field with $\mu T/\sqrt{Hz}$ sensitivity. The second figure of merit is the frequency at which these signals can be measured. We measured both DC and higher frequency field modulation up to 1 kHz but have not fully characterized the highest frequency possible to measure. We hypothesize it is likely limited by the excited state lifetime of the system, which is comparable to other Yb(III) complexes (μs to ms). The third figure of merit is the distance at which a magnetic field can be measured, namely the sensor-sample distance. Broadly speaking, the sensor-sample distance represents the effective geometry of a given magnetic sensor. In the context of nanoscale imaging, where magnetometers are used to detect single spin fields, it is crucial that the magnetic field sensor can capture the dipole field, which decreases with the cubed distance. Here, systems with high number densities of magnetically sensitive molecules may provide an advantage. For example, (thiolfan)YbCl(THF) can be concentrated to give an optical density of 1 in a thin 0.2 mm path length cuvette, effectively providing a sensor to sample distance that is considerably shorter than current AVC technologies.

We note that real quantum sensing technologies operate through modulation of ground-state quantum coherences, prepared through optical and microwave pumping, and readout through changes in absorption, polarization, or fluorescence intensity. Besides AVCs, other spin-based magnetometers include nitrogen vacancies in diamond and color centers in crystal environments, both of which are also enabled by optical state preparation of pure quantum states that enable extraordinary sensitivity[45][46]. Compact designs of AVCs that are widely used in miniature circuits demonstrate an optimal sensitivity of 50 $pT/\sqrt{Hz}$ with the most sensitive atomic optical magnetometer exceeding a 10^{-15} $T/\sqrt{Hz}$ sensitivity[47][20][18]. The typical sensitivities of magnetic sensing based on single nitrogen vacancy in diamond range from tens of $\mu T/\sqrt{Hz}$ for DC fields to tens of $nT/\sqrt{Hz}$ for AC fields[48]. To be

competitive with the sensitivities of these devices would require a state preparation and readout of spin superpositions in the electronic ground state that has yet to be shown in a liquid or glass environment. Nevertheless, a simple MCD-based magnetometry method with (thiolfan)YbCl(THF) puts us at a comparable sensitivity to other known spin-based magnetometers, such as Hall-effect sensors[49][50].

Based on the way we measure magnetic field, the signal depends on the amount of Zeeman splitting and how steep our absorption feature is. Here is a detailed derivation on the mathematical limit to the sensitivity of an MCD-based method.

The absorption of (thiolfan)YbCl(THF) can be expressed as a Lorentzian

$$\alpha(x, x_0) = \frac{a}{\pi} \frac{\frac{1}{2}\Gamma}{(x - x_0)^2 + \left(\frac{1}{2}\Gamma\right)} + c. \tag{3.7}$$

In this equation, a is a scaling factor, Γ is FWHM, x_0 is the center frequency, and c is a constant offset to account for background. The MCD signal is a subtraction between the absorption of σ^+ and σ^- light, which only differ in their center frequency by $\Delta x = g_{\text{eff}}\mu_{\text{B}}B$. Thus, the MCD absorption signal can be expressed as

$$M(x, B) = \alpha(x, x_0 + \Delta x) - \alpha(x, x_0 - \Delta x) \tag{3.8}$$

where $\alpha(x, x_0 \pm \Delta x)$ indicates the sample absorption with $\sigma^\pm$ light.

$$\alpha(x, x_0 \pm \Delta x) = \frac{a}{\pi} \frac{\frac{1}{2}\Gamma}{(x - (x_0 \pm g_{\text{eff}}\mu_{\text{B}}B))^2 + \left(\frac{1}{2}\Gamma\right)} + c. \tag{3.9}$$

The larger the B field applied, the further the σ^+ and σ^- absorption peak is split, the larger the MCD signal is. We can backtrack the strength of B field from the measured MCD signal if we know the factor g_{eff}. For small static magnetic field, we perform a Taylor expansion

$$\begin{aligned} M(x, B) &= \alpha(x, x_0 + \Delta x) - \alpha(x, x_0 - \Delta x) \\ &= \alpha(x, x_0) + \frac{\partial \alpha(x, x_0)}{\partial x_0}\Delta x - \alpha(x, x_0) - \frac{\partial \alpha(x, x_0)}{\partial x_0}(-\Delta x) \\ &= 2\frac{\partial \alpha(x, x_0)}{\partial x_0} g_{\text{eff}}\mu_{\text{B}}B. \end{aligned} \tag{3.10}$$

The MCD signal $M(x, B)$ is proportional to the applied static magnetic field B. The sensitivity is described by the slope

$$k(x, x_0, g_{\text{eff}}) = 2\frac{\partial\alpha(x, x_0)}{\partial x_0} g_{\text{eff}}\mu_{\text{B}}B \tag{3.11}$$

where

$$\frac{\partial\alpha(x, x_0)}{\partial x_0} = \frac{a}{\pi}\frac{\Gamma(x - x_0)}{\left((x - x_0)^2 + \left(\frac{1}{2}\Gamma\right)\right)^2}. \tag{3.12}$$

With a laser frequency set at $x = x_0 + \frac{\Gamma}{\sqrt{12}}$, this value reaches a maximum

$$\max\left(\frac{\partial\alpha(x, x_0)}{\partial x_0}\right) = \frac{a}{\pi}\frac{\Gamma\frac{\Gamma}{\sqrt{12}}}{\left((\frac{\Gamma}{\sqrt{12}})^2 + \left(\frac{1}{2}\Gamma\right)\right)^2} = \frac{3\sqrt{3}}{2}\frac{a}{\pi}\frac{1}{\Gamma^2}, \tag{3.13}$$

and the slope is

$$k|_{x=x_0+\frac{\Gamma}{\sqrt{12}}} = \frac{3\sqrt{3}a\mu}{\pi}\frac{g_{\text{eff}}}{\Gamma^2} \propto \frac{g_{\text{eff}}}{\Gamma^2}. \tag{3.14}$$

Thus the sensitivity of the absorption measurement is proportional to the g_{eff} factor of the driven transition and is inversely proportional to the square of the linewidth Γ. This indicates that for transitions with the same oscillator strength, narrowing the linewidth by half will increase the sensitivity by a factor of four, motivating the need for further chemical insight into synthesis and post-synthesis methods that narrow optical transitions.

CHAPTER 4

Spectral hole-burning (SHB)

In order to further examine the homogeneous linewidth under the inhomogeneously broadened 151 GHz linewidth and search for a narrower linewidth for magnetic sensing and potential qubit state preparation, we cooled the sample down to 77 K and performed a spectral hole-burning experiment. Spectral hole-burning is the frequency-selective bleaching of the absorption spectrum of a material, which leads to increased transmission (a "spectral hole") at the selected frequency[51]. The basic idea is to selectively deplete some population from the ground state of a certain group of molecules with a strong pump laser and then try to probe this same set of molecules with a weak probe laser. If the probe can interact with the same transition in the same group of molecules that the pump is addressing, it will detect the population depletion generated by the strong pump and it will be absorbed less. In other words, the sample is now more transparent to the probe laser. It is like we burn a spectral hole at the specific frequency with the pump laser. Assuming that the linewidth of the laser is narrower than the natural linewidth of the sample, the spectrum we obtain from this SHB experiment is purely homogeneously broadened because in this case, the pump and probe are only addressing a subset of molecules that have the same transition energy.

4.1 Experimental setup

The optical setup of SHB experiment is shown in Figure 4.1. We used a tunable narrow band CW laser (M Squared SolsTis Ti:Sapph laser) and a home-made external cavity diode laser (ECDL) as the laser sources. The laser beam was split into two paths by a polarizing beam

splitter, one for the pump and the other for the probe. The frequency of each beam was modulated by an acousto-optic modulator. The quarter waveplate controlled polarization of each beam. The beams then overlapped at the sample, which was held in a 0.2 mm cuvette in a cryostat (ST-100 continuous flow optical cryostat system from Lake Shore Cryotronics). The pump and probe beams were measured by photodetectors (PDA36A, PDA8A, PDA10A2 from Thorlabs). The sample we used was typically 30 mM (thiolfan)YbCl in 2-MeTHF.

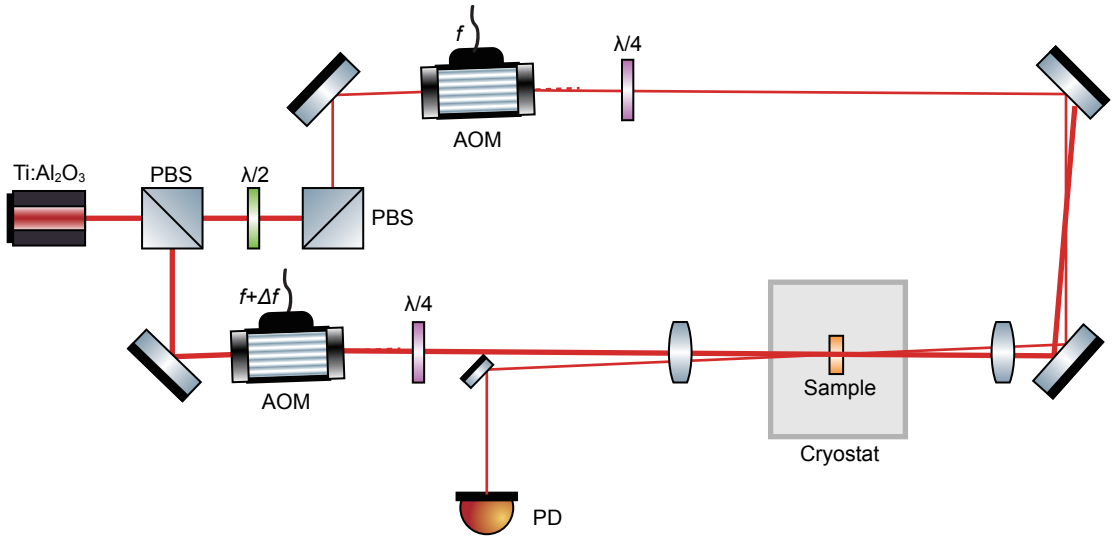

Figure 4.1: Optical setup of the SHB experiment. The laser source can be either a Ti:Sapph laser or a home made ECDL.

To search for the desired signal, the experiment needs to last for months, which means the sample needs to remain frozen for that duration. One 50 L dewar of liquid nitrogen typically lasts for 10-14 days, after which a refill is necessary to keep the experiment running. During a refill, we first disconnect the transfer line from the cryostat and then pour liquid nitrogen into the cooling tube of the cryostat using a funnel to keep the sample cold while we refill the liquid nitrogen dewar. While refilling, we need to clean any ice formed on the transfer

line with wipes and a heat gun to prevent them from blocking the transfer line. After the refill, the pressure in the dewar is typically low and takes a day to pressurize to 4-5 psi. We use nitrogen gas to pressurize the dewar to ensure constant liquid nitrogen flow to cool our sample. We have written a Python code to monitor the temperature and send alarms when the cooling fails. We have also attached electric valves to the dewar so that we can remotely pressurize the dewar. The longest experiment we have conducted lasted for 104 days.

The SHB spectrum can be directly measured by scanning the frequency of the pump while measuring the transmission of the probe. We use a compact FPGA-based pulser board, which was developed by Thaned Pruttiversan[52], to generate modulated RF signals which are then amplified by an amplifier (ZHL-2 from Mini-Circuits). The amplified RF signal is used to drive the AOMs. Pump beam is modulated at 1 kHz with depth of 0.6 MHz. The probe signal is read from an oscilloscope (DSO-X 2014A from Agilent Technologies) which is averaged 4000 times.

In order to increase the signal-to-noise ratio, we used a lock-in amplifier (SR830 DSP from Stanford research systems) for lock-in detection. The idea is to dither the pump at a certain frequency and only care about the measured probe signal at this frequency, thus efficiently rejecting all other frequency components of noise. In this way people can increase their signal-to-noise ratio by a factor of 1000. Our pump beam was dithered at 25 kHz and probe was slowly scanning at 0.5 Hz over 0.6 MHz. A function generator (332220A from Agilent) generated the dithering signal which was split into two channels. One channel was used to control the pump AOM via a voltage-controlled oscillator(VCO) (ZX95-200-S+ from Mini-Circuits), while the other channel served as a reference for the lock-in amplifier. The lock-in amplifier multiplied the reference signal with the measured probe signal to produce a DC lock-in signal.

4.2 Results

We first tried SHB experiment at room temperature with similar setup. Sample we used was 3 mM (thiolfan)YbCl(THF) in a 1 cm cuvette. Ti:Sapph laser was used and the pump beam power was around 10 mW, probe beam power was around 0.3 mW. We explored laser frequency, polarization, external magnetic field, pump probe beam propagation direction, sweeping/modulation frequency, laser power and beam size but was not able to obtain any expected pump-probe signal. The reason is likely to be that molecules quickly dephase due to frequent collisions in liquid at room temperature. Collisions can be suppressed by freezing the liquid sample to glass form.

4.2.1 Probe transmission change while chopping pump beam

2-MeTHF was used as the solvent for low temperature measurements because it can form a nice glass. By quickly switching on and off the pump beam, the intensity change in the probe beam was detected after subtracting the scattering background. When pump and probe beams are at the same frequency and polarization at the sample, the probe beam is more transmitted with the presence of a strong pump beam, whereas if the pump beam is switched off, the probe beam is less transmitted. Figure 4.2 shows the percentage change on transmitted probe intensity. Although the change is tiny but it is promising considering that it only appears when the pump and probe beam are on resonance with the sample. This laser frequency dependence assures that it is from light-molecule interaction instead of pure scatter noise.

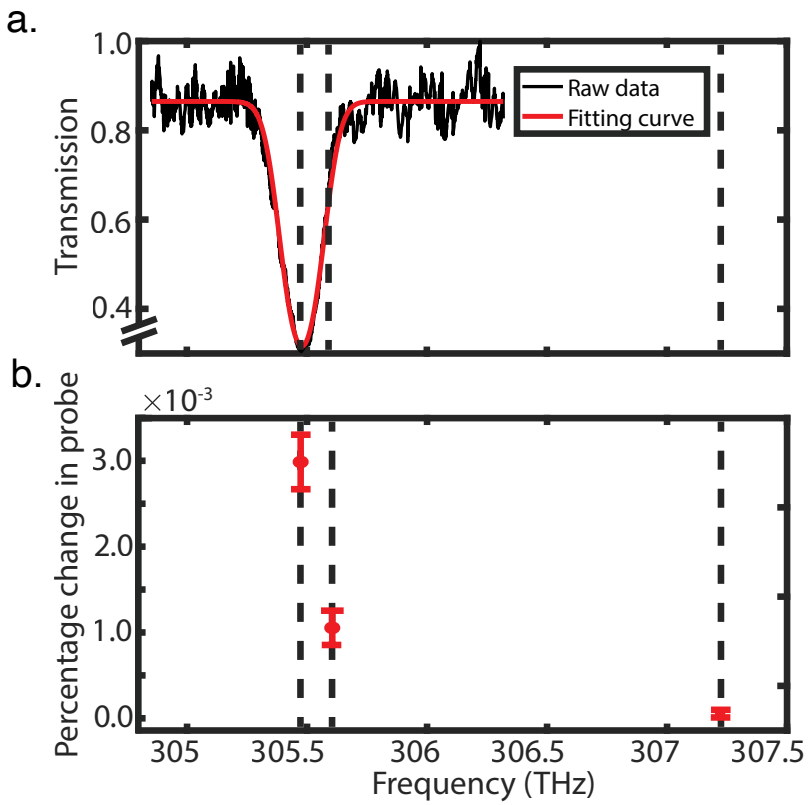

Figure 4.2: Probe transmission change while chopping pump beam. Laser source is Ti:Sapph, pump beam power is 10 mW and probe beam power is 0.3 mW. Both pump and probe are vertically polarized and are at same frequency. Sample we used is (thiolfan)YbCl in 2MeTHF cooled to liquid nitrogen temperature (77 K). The upper figure is an absorption spectrum of the sample at 77 K and lower figure is transmitted probe signal change at various laser frequency.

4.2.2 SHB spectrum

Not satisfied with just a percentage change in probe beam intensity, we want to know the lineshape of this hole burned by the strong pump beam. To do that probe beam's frequency is fixed as we sweep pump beam's frequency. We then measure the probe beam intensity as a function of the frequency offset between pump and probe. We choose to sweep pump

beam to eliminate the intensity change from the AOM as we sweeping it. Since probe beam's frequency is fixed, its intensity is fixed and does not change with the offset frequency between pump and probe.

Figure 4.3 a shows the electronic structure of the molecule and the transition we are addressing with pump and probe beam. Due to the non-zero ambient magnetic field and zero field Zeeman splitting, ground and excited state doublets are split. With a certain frequency and polarization, pump beam can only talk to a specific Zeeman transition of a small portion of the molecules who are on resonance with the narrow pump laser. It will deplete some population on one ground Zeeman state of the transition it addresses so that an imbalance between the ground state Zeeman levels is created. This can be imagined as "state preparation". Probe beam can talk to the same transition of the same molecules only if it have the same frequency and polarization as the pump beam. If polarization is same but frequency is different, probe beam will talk to another assemble of molecules. If polarization is orthogonal but frequency is same, it will not be able to address the specific Zeeman transition of the molecules pump beam is addressing.

Figure 4.3 b shows the probe transmission vs pump-probe offset frequency. When the polarization of pump and probe are parallel, probe beam can address the population depleted by the strong pump beam so its more transmissive. In other words, probe can sense the spectral hole pump creates and the linewidth of the peak is 99 ± 4 kHz (fitted with Lorentzian function). When polarization of pump and probe are orthogonal, the probe beam will not address the same transition as the pump beam, so the transmission is barely influenced by pump beam and the peak is suppressed. This 99 ± 4 kHz linewidth sets the upper limit of the natural linewidth of the transition.

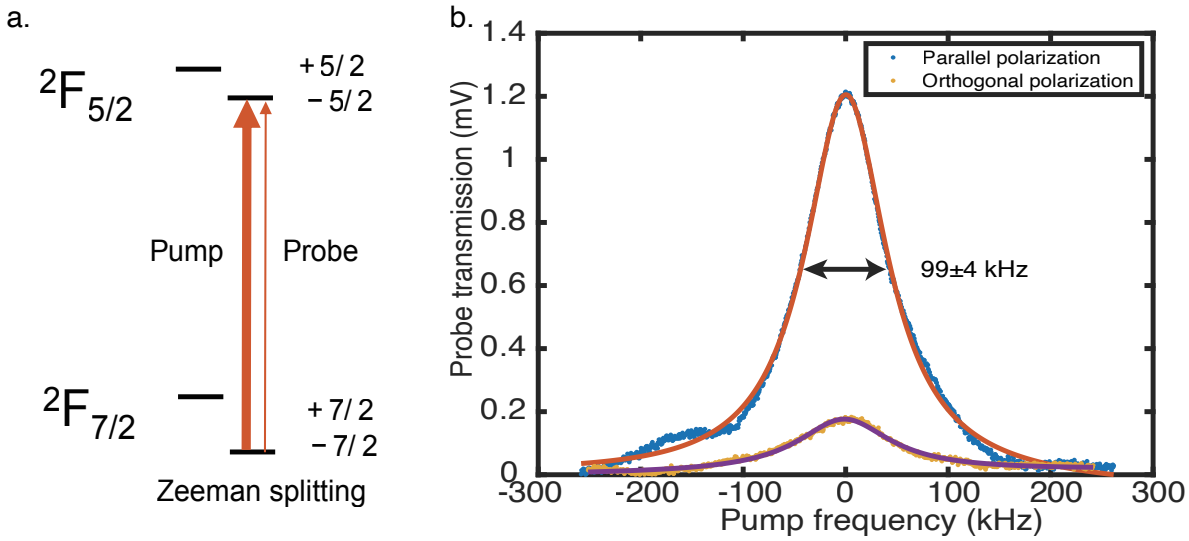

Figure 4.3: Spectral hole burning (SHB) spectra. a. Pump beam and probe are addressing the same transition of same molecular assembly. b. Probe transmission as a function of pump frequency offset. All SHB data is taken under liquid Nitrogen temperature with 30mM ThiolfanYbCl in 2-MeTHF. Pump beam is circularly polarized. Pump power is around 8 mW and probe power is around 0.7 mW. The spectrum is measured with probe polarization parallel and orthogonal to pump beam polarization. The FWHM of the spectrum is 99 ± 4 kHz.

4.2.3 Pump efficiency

4.2.3.1 Number of photons per molecule

To find if our pump beam is strong enough, we calculated the number of photons absorbed per molecule per second.

Pump power	P	8 mW
Beam radius	r	0.25 mm
Single photon energy	$h\nu$	2.02×10^{-19} J
Photon per second	$N_{\mathrm{p}} = \frac{P}{h\nu}$	3.95×10^{16} s^{-1}
Molecular concentration	n	30 mM $= 1.81 \times 10^{19}$ cm^{-3}
Cuvette path length	L	0.2 mm
Volume	$V = L\pi r^2$	3.93×10^{-11} m^3
Number of molecules on resonance in volume	$N_{\mathrm{m}} = \frac{1}{2} nV \frac{\Delta f_{\mathrm{h}}}{\Delta f_{\mathrm{inh}}}$	2.35×10^8
Number of photons per second per resonant molecule	$n_{\mathrm{p}} = \frac{N_{\mathrm{p}}}{N_{\mathrm{m}}}$	1.68×10^8 s^{-1}

Table 4.1: Number of photons absorbed per resonant molecule per second.

Since the absorption spectrum is 151 GHz and is inhomogeneously broadened, only an subset of molecules are on resonance, so we need a factor $\frac{\Delta f_{\mathrm{h}}}{\Delta f_{\mathrm{inh}}}$ where Δf_{inh} is the inhomogeneous linewidth 151 GHz and Δf_{h} is the homogeneous linewidth ∼100 kHz. The factor $\frac{1}{2}$ in front accounts for the fact that only half of the population is on resonance with the specific polarization. Since the number of photons per second per resonant molecule is way bigger than the homogeneous linewidth measured (100 kHz), this means we are saturating the transition with 8 mW pump.

4.2.3.2 Population imbalance

With the SHB spectrum we measured in figure 4.3 b, we can calculate how much population imbalance between the ground Zeeman doublet was created by the strong pump, or how much population was removed from the addressed ground Zeeman level.

At 77 K, we can assume the ground state Zeeman doublet $^2\mathrm{F}_{7/2}, m_{\mathrm{j}} = \pm 7/2$ are equally

populated. This Zeeman doublet is defined as our qubit and we call $m_{\mathrm{j}} = -7/2$ state $|0\rangle$ and $m_{\mathrm{j}} = +7/2$ state $|1\rangle$. The transition from $|0\rangle$ to excited state $^2\mathrm{F}_{5/2}, m_{\mathrm{j}} = -5/2$ can only be driven by σ^+ light and transition from $|0\rangle$ to excited state $^2\mathrm{F}_{5/2}, m_{\mathrm{j}} = +5/2$ can only be driven by σ^- light. The cross transitions will be super weak due to the high spin number change. This way we can selectively talk to each qubit level with laser polarization control. Our pump is only addressing one of the two states with certain circular polarization. Without loss of generality, we can assume the pump laser is addressing state $|0\rangle$ for the following discussion.

In Figure 4.3 b, with the presence of the pump, transmission of probe increased 1.7‰(with baseline 688.6 mV). Transmission can be expressed as

$$\frac{I}{I_0} = e^{-\sigma n L} \tag{4.1}$$

where I is transmitted light intensity and I_0 is incident light intensity, σ is absorption cross section, n is molecular density and L is path length. The presence of strong pump will remove some population in state $|0\rangle$ such that n is decreased from probe's perspective and $\frac{I}{I_0}$ is increased. Taking derivative of equation 4.1 we get

$$\frac{dI}{I} = -\sigma L dn = -\sigma n L \frac{dn}{n} = \ln\left(\frac{I}{I_0}\right)\frac{dn}{n} \tag{4.2}$$

where $\frac{I}{I_0}$ is 0.3 in our experiment. After plugging in numbers we get

$$\frac{dn}{n} = \frac{0.0017}{\ln 0.3} = -0.0014 = -1.4‰. \tag{4.3}$$

This means the pump beam removed 1.4‰ population from state $|0\rangle$. In other words we create an 1.4‰ imbalance between state $|0\rangle$ and state $|1\rangle$. This is a weak demonstration of state preparation where we start from state ρ_{i}

$$\rho_{\mathrm{i}} = \begin{pmatrix} 0.5 & \\ & 0.5 \end{pmatrix} \tag{4.4}$$

and prepare it to state ρ_{f}

$$\rho_{\mathrm{f}} = \begin{pmatrix} 0.4996 & \\ & 0.5004 \end{pmatrix}. \tag{4.5}$$

From the perspective of spin, initially the average spin is $0.5 \times \frac{7}{2} - 0.5 \times 72 = 0$ and with the presence of pump the average spin is $0.5004 \times \frac{7}{2} - 0.4996 \times 72 = 0.0028$.

4.2.4 SHB hole area dependence

To further understand the SHB spectra, we measured the spectral hole area against various probe polarization and pump power. In order to get a better signal-to-noise ratio and a more stable spectrum, we used lock-in detection method described in Section 4.1. We measured the second order lock-in signal vs pump-probe frequency shown in figure 4.4 a. It should be a second derivative of the original lineshape (Lorentzian-like as shown in Figure 4.3 b). However, we figured the second order lock-in signal was better fitted with a Gaussian instead of a Lorentzian and its linewidth was broader than spectra measured without lock-in. The reason might be that the pump dither depth was not small enough (we did notice that bigger dither depth would produce a broader spectrum as shown in Figure 4.4 b) and some systematic responsive function of the lock-in amplifier. Although it can not capture the real linewidth, the signal is way more stable and stronger than measurements done without lock-in so that we can measure a small spectral hole created by a weak pump. Hole area is calculated according to the fitted peak height and FWHM.

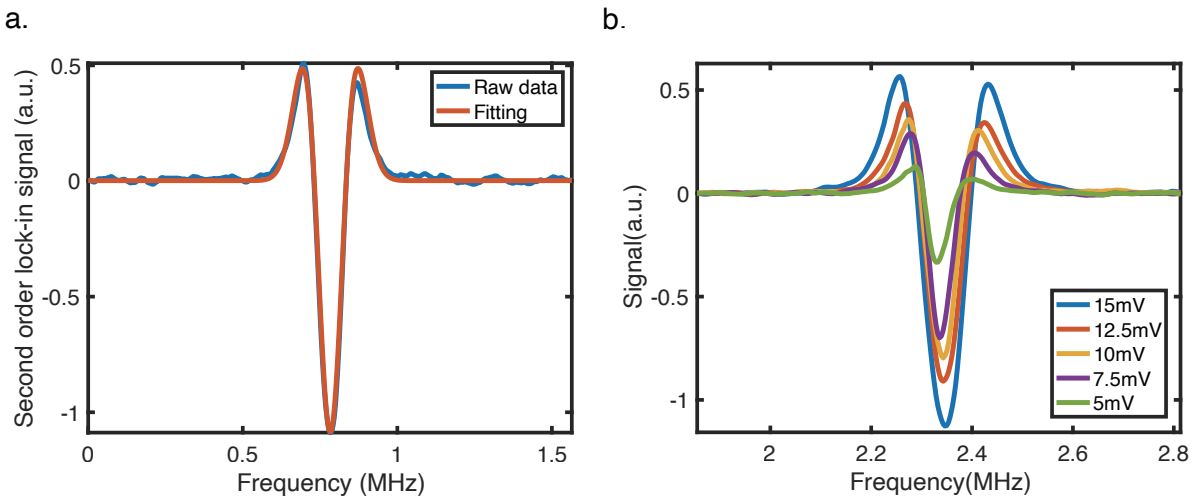

Figure 4.4: SHB spectra with lock-in detection. a. An example of the second order lock-in signal fitted with second order derivative of Gaussian. b. SHB spectra at various pump dither depth. The legend is the amplitude of the dither RF signal generated by a function generator.

To understand how the hole area changes as we gradually change beam polarization, we rotated the probe QWP step by step to measure the hole area at various QWP angle. 0 degree means probe polarization is the same as the pump polarization and $\pi/2$ degree means probe polarization is orthogonal to pump polarization. Figure 4.3 b demonstrates that the hole area depends on the polarization overlap between pump and probe beam. The hole area maximize at around 0 degree and minimize at around $\pi/2$ degree.

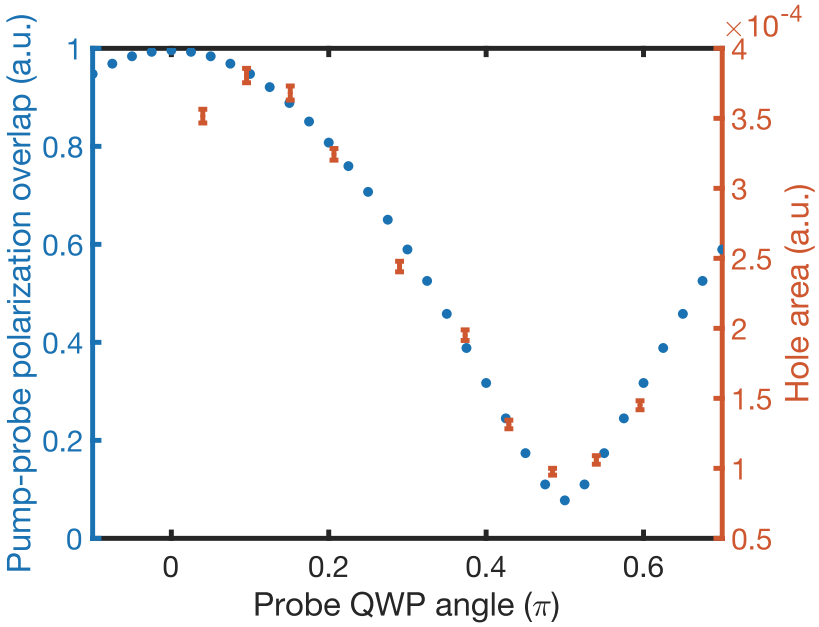

Figure 4.5: SHB hole area vs probe polarization. Pump beam is circularly polarized. The probe QWP modulates the polarization of the probe beam. With a $\pi/2$ degree rotation it changes the probe polarization from same to pump polarization to orthogonal to pump polarization. Orange data with error bar is measured hole area and blue dots are calculations of pump-probe polarization overlap.

We can calculate the polarization overlap as a function of the probe QWP angle with Jones matrix[53]. The pump polarization can be expressed as

$$|R\rangle = \frac{1}{\sqrt{2}}(|H\rangle - i\,|V\rangle) = \frac{1}{\sqrt{2}}\begin{pmatrix} 1 \\ -i \end{pmatrix} \tag{4.6}$$

where $|R\rangle$ means its right-hand polarized. $|H\rangle$ is horizontal polarization and $|V\rangle$ is vertical polarization. Initially probe beam is vertically polarized. After passing a QWP with fast

axis at angle θ with respect to the horizontal axis, its polarization can be expressed by

$$|P(\theta)\rangle = M\,|V\rangle = \exp^{-\frac{i\pi}{4}} \begin{pmatrix} \cos^2\theta + i\sin^2\theta & (1-i)\sin\theta\cos\theta \\ (1-i)\sin\theta\cos\theta & \sin^2\theta + i\cos^2\theta \end{pmatrix} \begin{pmatrix} 0 \\ 1 \end{pmatrix}. \tag{4.7}$$

Then the polarization overlap $f(\theta)$ between pump and probe beam is

$$f(\theta) = |\,\langle R|P\rangle\,|^2. \tag{4.8}$$

But we also need to consider the finite angle between pump and probe beam and other imperfect alignment of optical components and windows. This explains the slightly off between equation 4.8 and measured raw data in figure 4.5. But it does explain well the main trend.

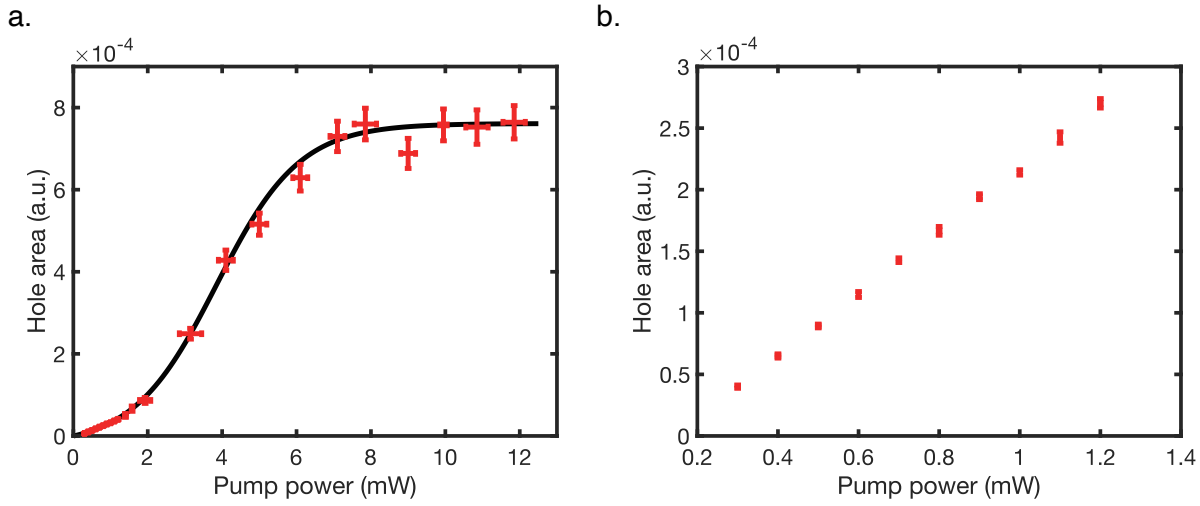

Figure 4.6: SHB hole area vs pump power. SHB spectra were measured by lock-in detection and the second order lock-in signal is fitted by the second order derivative of Gaussian function. Hole area is then calculated from the fitted hole height and FWHM. a. Hole area vs power from 0.25 mW to 12 mW. Data from 1.5 mW to 12 mW were measured using Ti:Sapph and data below 1.5mW were measured by ECDL. Data is fitted with a Fermi function. b. A zoom in view of a. It was measured with ECDL.

We also measured the hole area vs pump power which is shown in Figure 4.6. We can

see as pump power increases, the hole size increases, meaning a stronger pump will deplete more populations in the ground state. But this effect eventually plateau at around 8 mW pump power, which means it reaches saturation. At low pump power, the hole size is linear to pump power which is shown in Figure 4.6 b.

4.3 Linewidth broadening

Broadening mechanisms are typically divided into two categories: homogeneous broadening and inhomogeneous broadening. Homogeneous broadening usually means each molecule is broadened in the same way by the same mechanism, like collision broadening and natural lifetime broadening. Inhomogeneous broadening means each molecule has a slightly different transition energy and the total absorption is an average of the assemble. It can arise from fluctuations and disorders in local environments.

4.3.1 Laser linewidth

Before talking about the broadening mechanisms, it is worthwhile to first know the linewidth of the laser we were using to do all the measurements. The way to measure the linewidth of a laser is to split the light and add a delay in one path, then measure the beat-note between them. However this will need long fibers. Since we have two lasers, Ti:Sapph and ECDL, we can measure the beat-note between them and the shape of that beat-note will be a convolution of the lineshape of the two lasers. We combined the two laser beam with a beam splitter and measured the signal with a fast photodetector. We then used a spectrum analyzer ((Agilent Technologies N9010A) to convert that signal to frequency domain. Figure 4.7 shows the beat-note shape when measured with resolution bandwidth 30 kHz, where the peak shape is not well resolved. So we know that the beat-note width is less than 30 kHz and the linewidth of both lasers are below 30 kHz, which is narrower than the 99 kHz SHB linewidth we measured. So the 99 kHz wide SHB spectrum is not dominated by laser

linewidth.

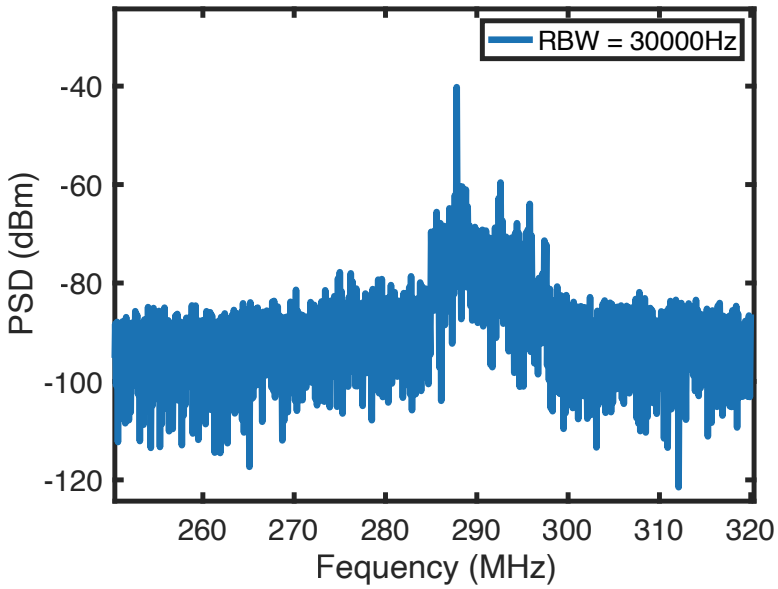

Figure 4.7: Beat-note between Ti:Sapph laser and the ECDL laser. They both were tuned to around 305.47 THz. The frequency difference is around 270 MHz so we see a beat-note at around 270 MHz. It was measured with resolution bandwidth (RBW) 30 kHz.

4.3.2 Homogeneous broadening

4.3.2.1 Power broadening

The linewidth of an absorption spectrum can be power broadened and it is well described by the power broadening model of two-level system[51]

$$\Gamma_{\mathrm{P}} = \Gamma_0(1 + I/I_{\mathrm{sat}})^{1/2} \tag{4.9}$$

where Γ_0 is the natural linewidth, I is the laser intensity, I_{sat} is the saturation intensity of the transition and Γ_{P} is the power broadened linewidth. In the lower pump power range where the hole area is linear to pump power, the system is not saturated so the power broadening

can be ignored.

4.3.2.2 Broadening from vibrational and rotational states

Not like gas phase atomic systems, molecules have a vast number of vibrational and rotational states that can populate and decay into. These states will be thermally populated so the absorption lineshape is broadened from the sum over all final states and over all initial states weighted by their Boltzmann populations. In our system we do not have the ability to resolve vibration states. But theoretical calculation can provide a good reference on the vibration and rotation structures and if possible, cold temperature gas phase molecular spectroscopy can be done in cryogenic chamber[56].

4.3.2.3 Collision broadening

Several dynamical mechanisms can potentially contribute to homogeneous line broadening: population relaxation $1/T_1$, pure dephasing $1/T_2^*$ and orientation relaxation Γ_{or}. Population relaxation comes from the finite lifetime of the excited states, which can have contributions from radiative decay, such as spontaneous emission, or non-radiative processes. Pure dephasing describes the randomization of phase as a result of molecular interactions like collision and environmental fluctuations. Orientation relaxation is caused by loss of angular correlation of an ensemble of dipoles. We can estimate the collision frequency to get a sense on the time scale of pure dephasing and orientation relaxation.

To calculate the collision frequency between one sample molecule and solvent molecules, we need to know the average velocity and mean free path of the sample molecule.

The mean free path can be calculated by

$$\ell = \frac{1}{n\sigma} \tag{4.10}$$

where n is number of THF per unit volume and σ is effective cross-sectional area for collision between sample molecule (with radius 0.8 nm) and THF (with radius 0.125 nm [55]).

v_{ave} can be estimated from diffusion coefficient D. According to Stokes-Einstein equation, the D of spherical particles through a liquid is

$$D = \frac{k_{\text{B}}T}{6\pi\eta r} \tag{4.11}$$

where k_{B} is Boltzmann constant, T is temperature, η is the viscosity and r is radius of the particle. With this the approximate diffusion coefficient of (thiolfan)YbCl in THF at room temperature is $D = 5.6 \times 10^{-10}$ m^{2}s^{-1} ($\eta = 0.48$ cp[54], $r = 0.8$ nm). Average velocity v_{ave} and diffusion coefficient D are related by

$$D = \frac{\ell v_{\text{ave}}}{3}. \tag{4.12}$$

In our system $\ell = 0.05$ nm, $v_{\text{ave}} = 33.4$ ms^{-1}. This velocity corresponds to a Doppler broadening of 50 MHz. It is calculated by

$$\Delta f_{\text{D}} = \sqrt{\pi \ln(2)} \frac{v_{\text{ave}}}{c} f_0 \tag{4.13}$$

where Δf_{D} is Doppler broadened full width at half maximum, c is speed of light and f_0 is center transition frequency. Note here Doppler broadening is inhomogeneous broadening. For comparison, the v_{ave} of free gas phase molecule with molar mass 893 g/mol at 293 K is around 83 ms^{-1}, which corresponds to 125 MHz FWHM at 305.6 THz. It is way bigger than liquid phase molecules because liquid systems are way denser more viscous so that velocity of molecules is slow. 50 MHz is small comparing to the broad 151 GHz room temperature absorption feature which supports that the peak is dominated by other broadening mechanisms. Our SHB measurements were done with counter-propagating pump and probe beam so it is Doppler free and we are doing it below glass forming temperature, so Doppler broadening can be ignored for our SHB spectra.

With mean free path ℓ and average velocity v_{ave}, collision frequency is calculated by

$$\Gamma = \frac{v_{\text{ave}}}{\ell}. \tag{4.14}$$

The collision frequency between sample molecule and THF is $\Gamma_{c1} = 670$ GHz, whereas collision frequency between sample molecules is $\Gamma_{c2} = 490$ MHz with 3mM concentration. The spectrum is collision broadened by

$$\Gamma_c = \Gamma_0 + 2\Gamma_c. \tag{4.15}$$

Since Γ_{c1} is way bigger than Γ_{c2}, the collisions are mostly from (thiolfan)YbCl(THF) - THF collision instead of (thiolfan)YbCl(THF) - (thiolfan)YbCl(THF) collision. This agrees with our concentration dependent absorption measurements where we measured the absorption linewidth of (thiolfan)YbCl(THF) in THF at room temperature from with 1 mM, 10 mM and 100 mM concentrations. The results are shown in Figure 4.8. We find little change in the observed linewidth, suggesting no sample-sample intermolecular contributions to the linewidth.

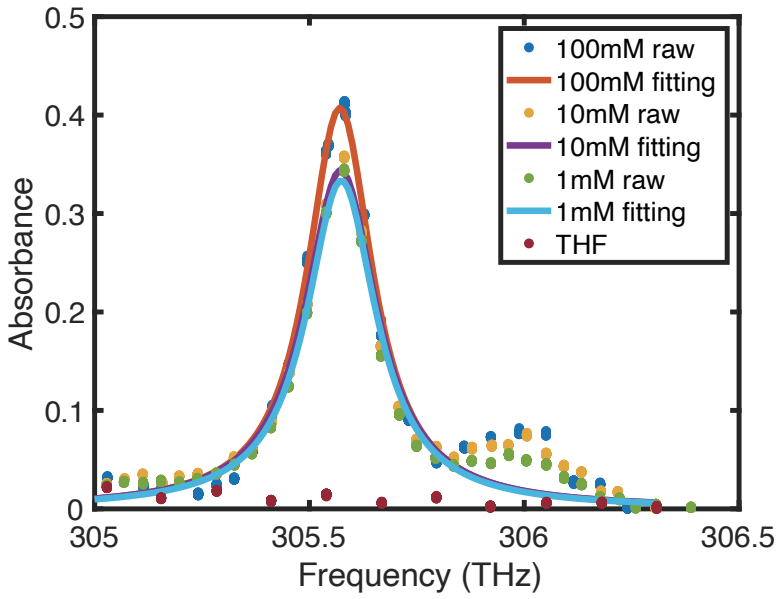

Figure 4.8: Room temperature absorption vs concentration. This is done with (thiolfan)YbCl(THF) in THF at 1 mM, 10 mm cuvette path length, 10 mM, 1 mm cuvette path length, 100 mM, 0.1 mm cuvette path length.

This Γ_{c1} = 670 GHz (thiolfan)YbCl(THF) - THF collision frequency agrees well with collision broadenings in room temperature liquid systems which is around 500 GHz to 1500 GHz[57]. However our room temperature absorption is 151 GHz which is already narrower than this collision effect. This suggests that collisions with solvent molecules wouldn't fully de-excite our inner f-f transition. To find out how much collision and thermal effect contribute to the linewidth, we did temperature dependent absorption measurement (Figure 2.6) which shows that as we cool the sample to glass form, the absorption spectrum narrows 30 GHz, which is one magnitude smaller than Γ_{c1}. One reason might be that the solvent molecules are 10 times lighter than our sample molecule. It also suggests that our transition is protected by the rigid ligand so that collision broadening is not as severe as calculated value.

4.3.2.4 Environmental fluctuation

The ambient magnetic field is measured by a magnetic field sensor (FGM3D/100 from Sensys GmbH) for 10 hours and the noise level is around 1×10^{-3} G. From the magnetic field sensitivity we measure before (chapter 3), this corresponds to a 6 kHz broadening.

4.3.3 Inhomogeneous broadening

Inhomogeneous broadening arises from different molecules having slightly different local environments, leading to a distribution of electronic energy gaps and an ensemble-averaged spectrum that is inhomogeneously broadened[58]. In liquid and solid system, the local environments are created by neighboring molecules and transition energy can be shifted by those intermolecular interactions like repulsive interactions from Lennard-Jones potential models, dispersive interactions from London forces and also Coulomb interactions caused by internal electric fields[59]. Due to the intrinsically disordered nature of glass and fluctuations in liquid system, different molecules may have a different transition shift such that the total ab-

sorption is inhomogeneously broadened. Our temperature dependent absorption experiment shows that the 151 GHz absorption line might be mainly inhomogeneous broadening. To study these interactions and inhomogeneous broadening, temperature dependent absorption measurement with solvent having different dielectric constant, polarity and polarizability can be done in the future.

On the other hand, Barry Li did some interesting calculations on the inhomogeneous linewidth of this liquid molecular system with point charge fluctuation model. In our system, the ferrocene backbone clips the metal center which makes the molecule rigid. The only 'loosing' part is the THF coordination. With a slightly different coordination angle and distance, molecular orbits and transition energies may change. Thus fluctuations of this THF coordination in liquid or disorders in glass can contributes to an inhomogeneous broadening. In the point charge model developed by Barry Li, the coordinated THF is allowed to spatially fluctuate around its equilibrium position in a confined cubic box (Figure 4.9 a) and spin-orbit crystal field (SOCF) calculation is performed to find the energy levels for each THF position. We find that as the THF fluctuates, there is a strong ground-excited energy correlation between the states (1, 2) and (9, 10) (Figure 4.9 b). This high correlation feature suppresses inhomogeneous broadening and hence provides an ultra-narrow linewidth. The THF fluctuation can reproduce the measured linewidth as shown in figure 4.9 c. This suggests that our inhomogeneously broadened lineshape may come from the 'loosing' solvent coordination. Experimentally we do notice a slightly broadening in (thiolfan)YbCl in 2-MeTHF comparing to (thiolfan)YbCl in (THF), which indicates that solvent does contribute to the lineshape.

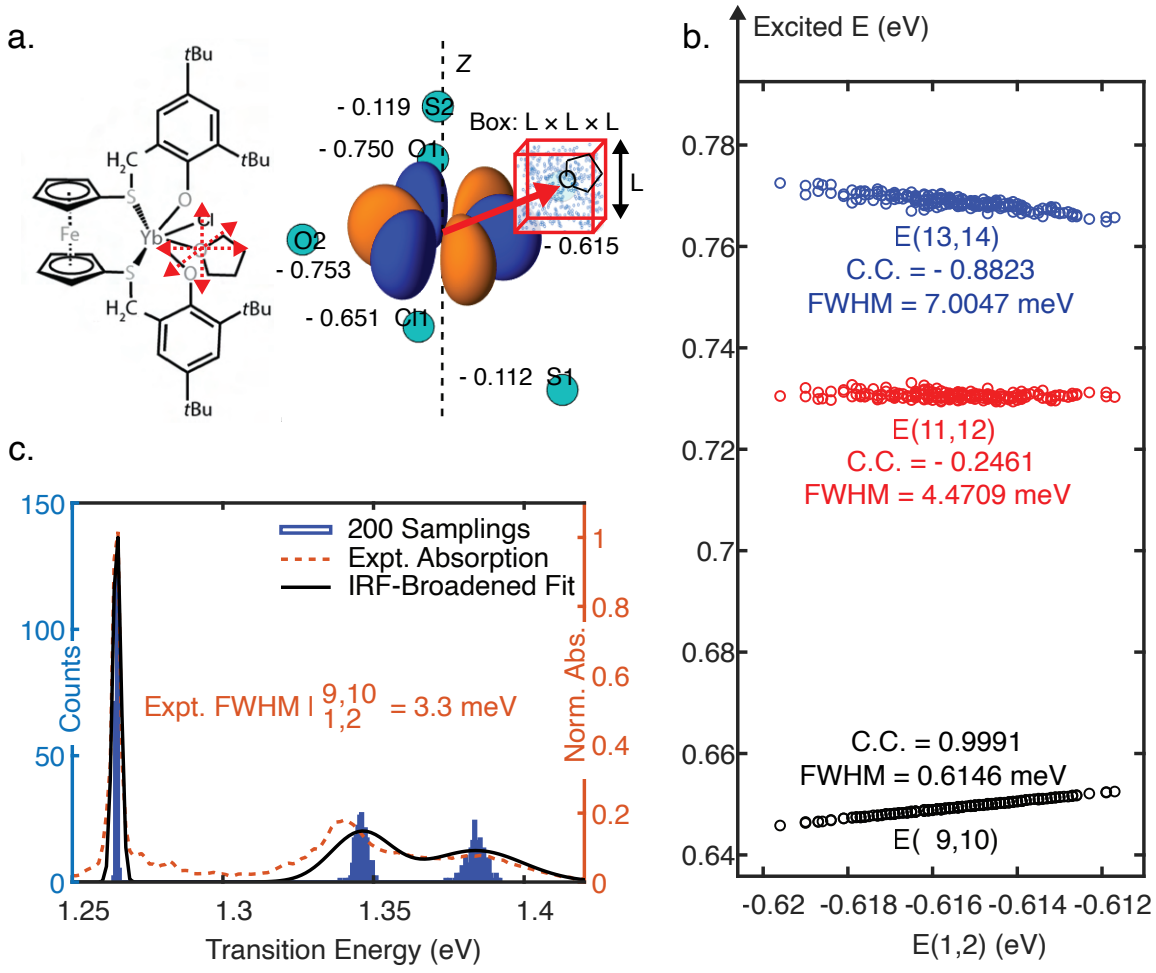

Figure 4.9: Energy shifts with coordinated THF fluctuation. a: Point charge model with THF movable. b: the correlation plot of E(9,10), E(11,12), and E(13,14) against E(1,2) of (thiolfan)YbCl(THF), illustrated with the correlation coefficients (C.C.). c: 200 samplings with an all-charge-moving model, the transition energy histograms are plotted and overlaid with experimental ones. These plots are made by Barry Li.

CHAPTER 5

Future directions with Yb complex

5.1 Electric field sensing

In addition to magnetic field sensing and imaging as demonstrated in Chapter 3, this room temperature liquid system can also be used for electric field sensing and imaging due to its ultranarrow absorption linewidth. When an external electric field is applied, the transition energy can split and shift. It is the electric-field analogue of the Zeeman effect. Electroabsorption/emission spectroscopy is a well-established technique and people have using it to study the physical properties of a sample using a well-characterized electric field[60][61][62] or to reveal information about an electric field using a reference sample with a well-characterized electric shift effect. For example, the Boxer Lab has established and utilized vibrational energy shift under electric field to quantify functionally relevant electric fields in proteins[63].

The energy shift under a static electric field is dependent on the dipole moment $\boldsymbol{d}$ and polarizability tensor $\boldsymbol{\alpha}$. The electric field induced energy shift is given by

$$h\Delta\nu = -\Delta\boldsymbol{d}\cdot\boldsymbol{E} - \frac{1}{2}\boldsymbol{E}\cdot\Delta\boldsymbol{\alpha}\cdot\boldsymbol{E} \tag{5.1}$$

where $h\Delta\nu$ is the transition energy shift, $\Delta\boldsymbol{d}$ is difference in dipole, $\Delta\boldsymbol{\alpha}$ is change in polarizability and $\boldsymbol{E}$ is the external electric field. Typically, two transparent electrodes spaced with a spacer of tens of micrometers are used to sandwich the sample, and a high-voltage supply is connected to the electrodes to provide a high electric field over the sample. The absorption spectrum is then taken and people fit the change in absorption ΔA with the first and second derivative of the absorption spectrum A to extract $\Delta\boldsymbol{\alpha}$ and $\Delta\boldsymbol{d}$[64]. The linear term $-\Delta\boldsymbol{d}\cdot\boldsymbol{E}$

will shift the transition to either higher or lower energy, depending on the orientation of $\boldsymbol{d}$. In liquid or glass, $\boldsymbol{d}$ is randomly orientated so it will broaden the absorption feature, which means that the change in absorption with/without an external electric field will be like the second-order derivative of the original lineshape. The quadratic term $-\frac{1}{2}\boldsymbol{E}\cdot\Delta\boldsymbol{\alpha}\cdot\boldsymbol{E}$ will shift the transition to the same direction, no matter how the dipole is orientated. Thus, the change in absorption with/without an external electric field will be like the first-order derivative of the original lineshape. The main experimental limitations are the uncertainties in determining the absorption lineshape and the magnitude of the electric field.

We have done a preliminary electroabsorption spectroscopy measurement with 10 mM (thiolfan)YbCl(THF) in a 1 mm cuvette at room temperature. We sandwiched the cuvette with two copper plates which were connected to a high-voltage power supply (PS350 Stanford Research). A 1 mm hole was drilled on the copper plates to do absorption spectroscopy. We measured the absorption with 2kV voltage applied onto the copper electrodes (3 mm apart). However we were not able to notice a difference with/without the external electric field. Based on our instrumental resolutions we figured the difference in dipole of our sample is less than 0.3 D. In order to resolve the electric field splitting, we can use transparent conductive material like ITO (Indium Tin Oxide) instead of copper as the electrodes to generate uniform electric field while letting through laser beams and reduce the space between the electrodes to increase the strength of electric field. We can also do lock-in detection to increase signal to noise ratio.

If we can accurately calibrate the electric shift of our sample, we can transform it into an electric field sensor capable of electric field sensing and imaging. Higher level theoretical calculation is still ongoing but with a point charge model, Barry Li calculated the difference in dipole to be $\Delta\boldsymbol{d} = 0.04$ D. This gives us some hint on the magnitude of electric field shift we should expect experimentally. If we only consider linear shift, for a dipole change of 0.04 D under 1 MV/cm electric field, it will produce an energy shift of

$$|\Delta\nu| = \frac{\Delta\boldsymbol{d}\cdot\boldsymbol{E}}{h} = 20 \text{ GHz} \tag{5.2}$$

In previous magnetic field sensing experiments, we were able to sense a 1 MHz shift with lock-in detection. If that is also true here, our sensitivity can reach down to 50 V/cm. This indicates that our sample has the potential to measure the electric field inside a protein where the electric field scale is MV/cm.

5.2 State preparation and measurement

In Chapter 4 we measured a ∼100 kHz extraordinarily narrow SHB spectrum by selectively deplete some population from one of the ground Zeeman levels. This is a beginning to state preparation and measurement. To implement this ground Zeeman doublet to be a two-level qubit system, we need ways to manipulate or shuffle population between the doublet.

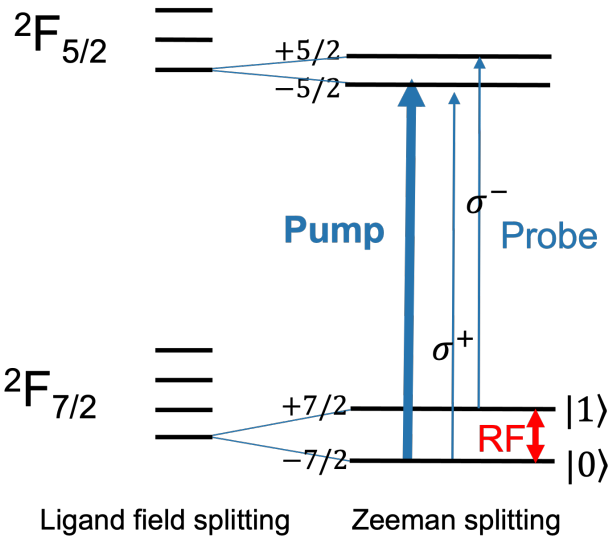

Figure 5.1: Qubit implementation with the ground Zeeman doublet. The levels are labeled with atomic notations for convenience because they are atomic like. But indeed they are molecular states with ligand and $5d$ mixings.

As shown in Figure 5.1, we can treat our ground Zeeman doublet as our qubit state:

$^2F_{7/2}$, $m_j = -7/2$ as $|0\rangle$ and $^2F_{7/2}$, $m_j = +7/2$ as $|1\rangle$. State $|0\rangle$ can be selectively addressed by a σ^+ light to the upper excited state $^2F_{5/2}$, $m_j = -5/2$ and state $|1\rangle$ can be selectively addressed by a σ^- light to the upper excited state $^2F_{5/2}$, $m_j = +5/2$. We can prepare the qubit to state $|0\rangle$ by pumping out the population in state $|1\rangle$ and vice versa. To manipulate populations between state $|0\rangle$ and $|1\rangle$, we can apply a RF field to drive transition between them. However, this is close to a $\Delta m_j = 7$ transition which is hard to drive. Fortunately our EPR spectrum shows resonance of this transition, which means this transition is not impossible to drive. EPR is done at 5 K with 3 mM (thiolfan)YbCl in 2-MeTHF. X-band EPR measures the resonance of 9.6 GHz microwave (MW). The magnitude of the MW radiation is governed by microwave power and the conversion factor of the resonant cavity, which manufacturer specs claim as 1.3 $GsW^{-1/2}$ for the resonator (Bruker ER 4116 DM). In EPR measurement, a MW power of 2.2 mW is used so the strength of the MW amplitude would be around 0.06 Gs. This gives us some guide on the strength of the applied RF field we need if we would like to drive this 'impossible' transition.

In our SHB experiment, we used 30 mM (thiolfan)YbCl in 2-MeTHF as our sample and cooled it to 77 K. If we can apply a RF field that matches the ground state Zeeman splitting and is strong enough, we should be able to notice a population change on state $|0\rangle$ and $|1\rangle$ with a weak probe. To do so we first applied an external magnetic field along laser propagation direction to split the Zeeman doublet. Since we know the ground state g-factor $g_g = 3.718$ pretty well from the EPR spectrum, we can calculate the ground state Zeeman splitting if we know the applied static magnetic field very well. We then applied a RF field orthogonal to the external field whose frequency was designed to match this Zeeman splitting. With the presence of pump and probe addressing the same transition, we want to measured a difference in the probe signal when the applied RF field is on resonance with the ground state Zeeman transition.

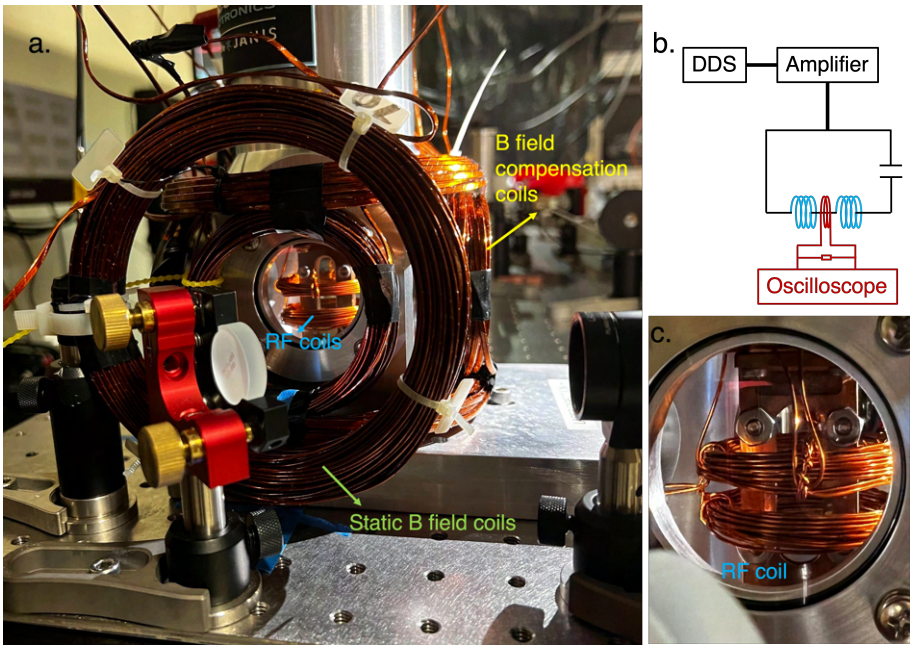

Figure 5.2: RF coils in the chamber. a. A picture of the coils inside the cryostat and outside the cryostat. b. Circuit to drive the RF coil and measure the RF field. c. A closer view to the RF coils.

As shown in Figure 5.2 a and c, we wrapped two coils along the vertical direction. Each was 24 turn with radius around 2 cm. A tunable capacitor was in series with the RF coils as shown in Figure 5.2 b. Network analyzer was used to measure the resonance frequency of this RLC circuit and it was around 1.6 MHz. We used the pulser board to generate the 1.6 MHz RF signal to drive the RF coils. A pick-up coil ($N = 2$ turns, radius 2 cm) was inserted between the RF coils to measure the electromagnetic field generated by the RF coils.

$$B_{\mathrm{RF}} = \frac{EMF}{2\pi f_{\mathrm{RF}} NA} \tag{5.3}$$

where EMF is the measured voltage amplitude, f_{RF} is the RF frequency, A is the coil area. We measured 6.3 V for the EMF at 1.6 MHz, which means the magnetic field amplitude of the RF field was 1.27 Gs. This is way bigger than the MW amplitude in EPR measurement.

We used a pair of coils along the laser direction to generate an external magnetic field

that split the Zeeman states to 1.6 MHz. Since we did not know exactly the strength of the magnetic field at the sample position, we swept the magnetic field while monitoring the probe intensity. We expected to notice some change in the probe intensity when the RF field was on resonance with the Zeeman levels. Unfortunately we was not able to notice any difference.

There are a couple things we can do to improve this experiment. First we need to get a better knowledge of the strength of the applied external magnetic field. This may involve placing an vacuum compatible magnetometer near the sample position and add some feedback control to actively cancel out ambient magnetic field fluctuation. Second we can try the same experiment at lower temperature like 5 K to reduce more vibrational freedoms. Third we can take advantage of the MW and B field generated by the EPR equipment. For instance, we can implement pump and probe lasers to the EPR setup to do SHB experiment. When the ground Zeeman transition is driven resonantly by the EPR setup, we would expect to measure some population difference with our pump-probe technique. Also it will help if we can get a crystallized sample instead of glass form where spins are randomly orientated.

5.3 Exploring more variants and surface implementation

To expand the family of ultranarrow species and investigate how factors such as rigidity, symmetry, and solvent environment affect the linewidth, it would be beneficial to synthesize additional variants of the Yb complex. This molecule was originally designed with Y center and utilized for catalysis[65]. we could explore the possibility of substituting the metal center with other lanthanides such as Er, Eu, Pm, Nd, Pr, as well as using alternative ligands aside from -Cl or -$N(SiMe_3)_2$. Additionally, since we suspect that solvent coordination may be a significant contributor to inhomogeneous broadening, we could try to find out ways to close that opening with a more rigid ligands.

Yi Shen is also investigating the possibility of implementing anchoring handles or linker

molecules to the benzene ring, allowing it to be attached to the surface of a substrate. If this can be achieved without destroying the ultranarrow atomic-like transition in the metal center, we could implement an array of molecular qubits for quantum sensing and even quantum computing. For instance, if our molecules can be grown on an ITO surface, we could apply an electric field through the ITO to perform electroabsorption/emission spectroscopy. Additionally, we can investigate the cross-talk between two molecules bounded next to each other. We could even attach the molecule to a silica chip with cavities and waveguides to build an on-chip quantum device.

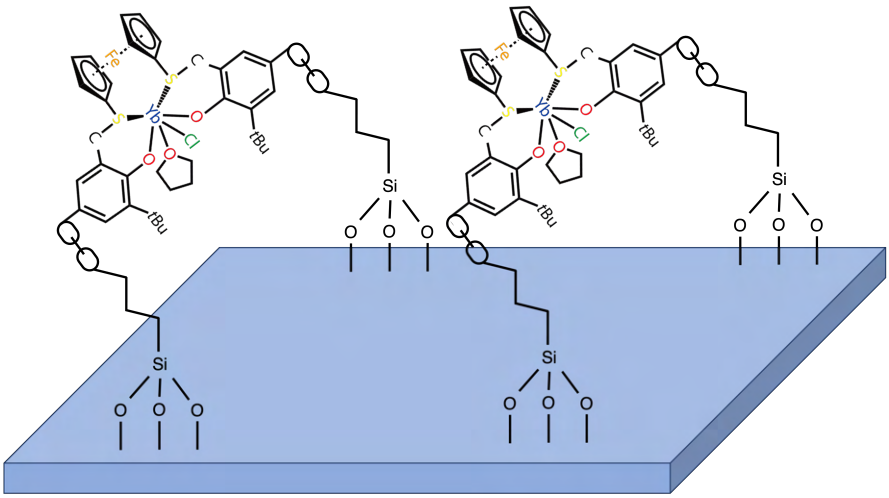

Figure 5.3: Schematic drawing of Yb based molecules anchored on substrate surface.

CHAPTER 6

Surface optical cycling centers (OCCs)

Repeatable, state-selective optical transitions are widely used for state preparation and measurement of qubits hosted by trapped atoms. Due to the vibrational structure that is introduced when trying to apply this technique to molecules, optical cycling is typically unavailable. However, recent works on laser cooling of polyatomic molecules[66, 67, 68] have successfully shown that optical cycling is possible in molecules with an alkaline-earth metal bounded to other chemical ligand with an oxygen (MO-R). More work has been done showing that the optical cycling property is maintained even attached to a variety of aromatic compounds[56]. Inspired by this, we propose building a candidate quantum system consisting of assembled monovalent molecules of alkaline-earth (AE)-oxide that are bond to a surface. This surface bounded OCCs are designed to be scalable and packed at high density with ability for fast and high-fidelity qubit operations and *in-situ* coherent transport of quantum information. Theoretical works has shown that MO- radical cycling center can be attached to R groups as large as the diamond or cBN surface[69]. Here we report our experimental effort toward building surface bounded OCCs and discuss the detection sensitivity limitations based on our current experiment apparatuses.

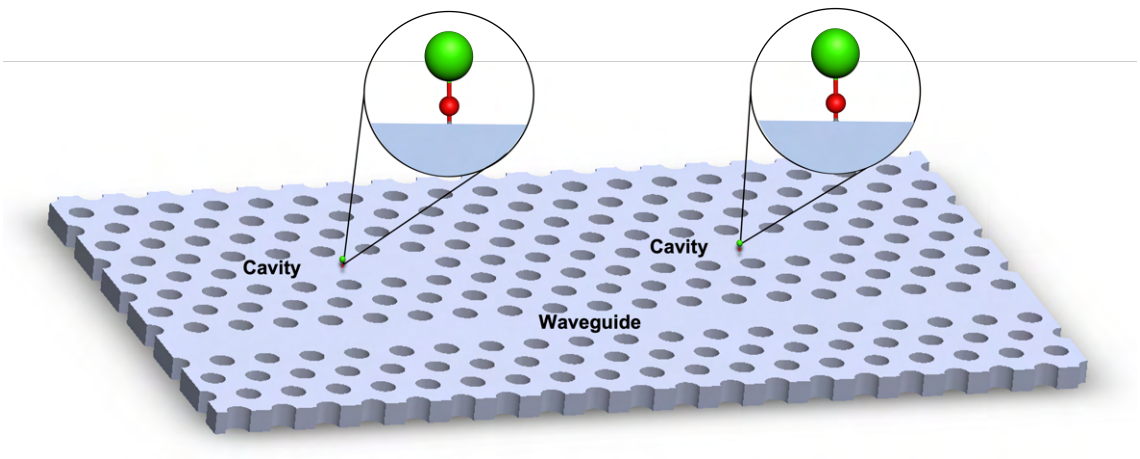

Figure 6.1: Schematic drawing of alkali based OCCs on silica chip. OCCs can be placed in a photonic waveguide, entangling two OCCs via photonic bus.

6.1 Experimental setup

The experimental setup and optics are shown in Figure 6.2 and 6.3. The laser we used is Sprit-OPA-30 pumped by a ytterbium doped solid state pulse amplifier. The chamber we used is a 2.75" flange multiplexer from Kimball Physics, which is pumped down to 10^{-7} to 10^{-8} torr by a turbomolecular pump TPS-compact from Agilent technologies. Signal is detected by a photonmultiplier tube H10682-210 from Hamamatsu. Temporal signal (lifetime) is detected with the multichannel picosecond event timer and time-correlated signal photon counting (TCSPC) module HydraHarp (1ps resolution) from PicoQuant.

There are 4 kinds of atomic sources imbeded in the CF nipple: Yb, Ba, Ca, Sr (from AlfaSources). They are held with a self-designed grabber and current can run through the atomic source tube to release the desired ultra-pure alkali metal when the required sublimation temperature is reached due to the activation current.

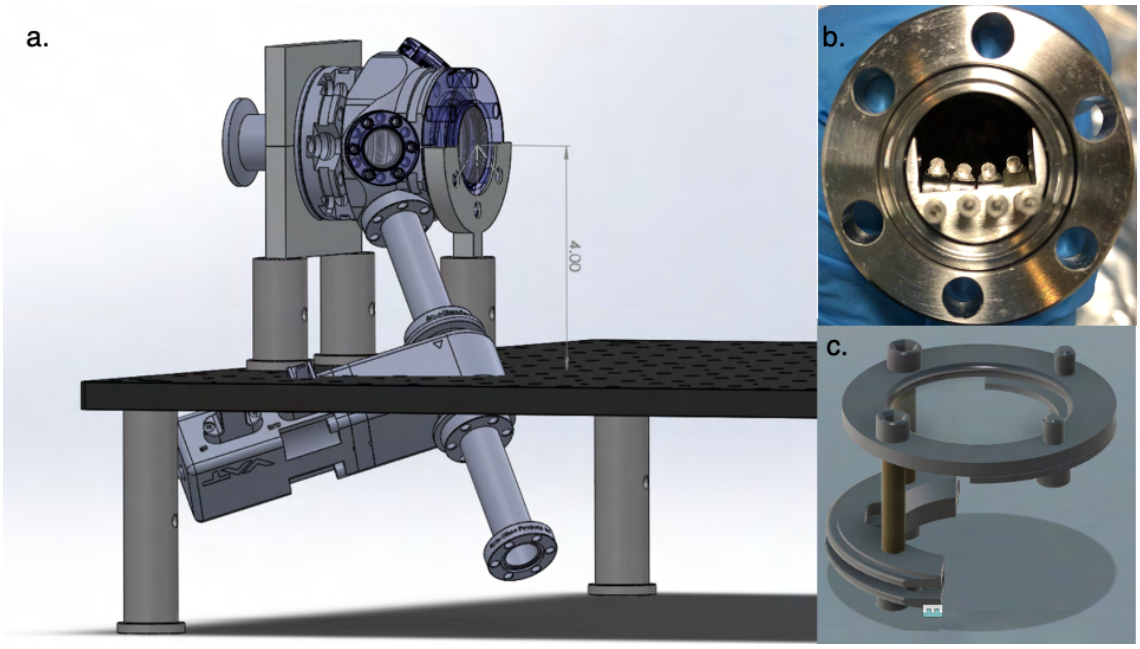

Figure 6.2: CAD drawing of experimental chamber and oven. a. CAD drawing of the chamber and atomic source (oven). b. 4 kinds of atomic sources are held by a self-designed spanner. From left to right they are: Yb, Ca, Sr, Ba. c: Substrate is held by a groove grabber inside the chamber.

The first lens (diameter $D = 1$ inch) which is closer to the chamber has f = 48 mm and the other one (diameter = 1 inch) has f = 30 mm. Distance from the substrate surface to the first lens is around $l = 60$ mm, from the first lens to the iris is around $l' = 230$ mm, from the iris to the second lens is around 58 mm and from the second lens to the detector is 70-75 mm. Magnification is roughly 5. When the iris is closed, the pin hole diameter is around $d = 500\ \mu m$ and the spot on the substrate is $118\ \mu m$. Depth of field is around 0.6 mm which is calculated by:

$$\text{Depth} = \frac{2l}{D}\frac{l}{l'}d \tag{6.1}$$

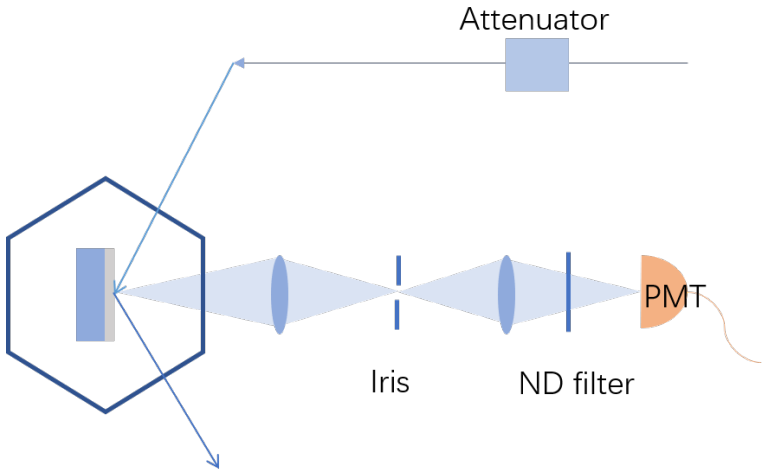

Figure 6.3: Schematic drawing of the experimental optics. The hexagon represents the chamber and there is a mirror at the back of the substrate. The laser reflects back from the substrate and the mirror.

The laser output wavelength ranges roughly from 310 nm to 3000 nm and its output power depends on the wavelength (Figure 6.4). Laser rep rate can go to 1MHz. Pulse duration is around 150 fs. The advantage of this laser is that it can scan over a broad range to find the transitions that we don't know the exact frequency. Once we find where the transition is, we can switch to a narrow band laser for higher power efficiency. Since the pulse laser has a short pulse duration, in frequency domain the laser is quite broad band, which means not all photons are useful for transition excitation and thus can cause background noise. The mirror at the back of the substrate is used to reflect the incoming light to reduce scatters in the chamber. This may not be the best way to reduce scattering light.

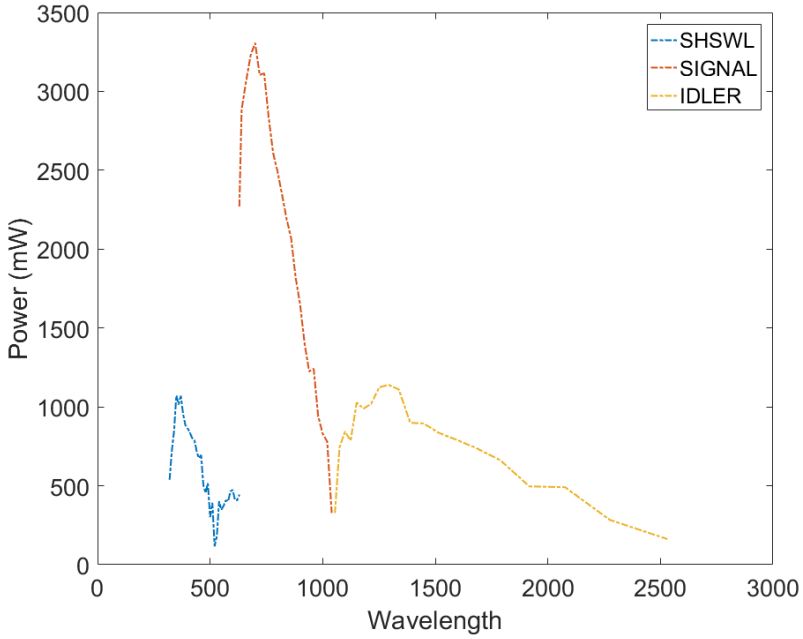

Figure 6.4: Ultrafast laser output power vs wavelength. This is approximately the best we can get. Experimentally due to alignment and optical components the power we can get is less than this.

6.2 Results

The goal of our research is to achieve state preparation and measurement with surface-bound alkaline-earth (AE) metal-based optical cycling centers (OCCs). The experimental setup involves depositing alkaline-earth atoms onto the diamond substrate using an atomic source. Atoms on ^3P state can replace the H in the OH group to form a metal-O-diamond (M-O-R) structure. An additional laser may be required to produce more ^3P state atoms. The first signal we need to see is the fluorescence from gas phase AE atoms near or on the substrate surface. Since the fluorescence is at the same frequency as the excitation laser, and as mentioned before, the background scatter from the excitation laser is inevitable, the main challenge is to improve the signal-to-noise ratio. While it is difficult to separate the

signal in frequency, it is feasible to separate them by time (Figure 6.5a). The photon counts are slightly higher during the arriving time 615 ns to 620 ns when the oven is on, indicating the presence of Sr atoms. However, the difference is quite small even in time domain.

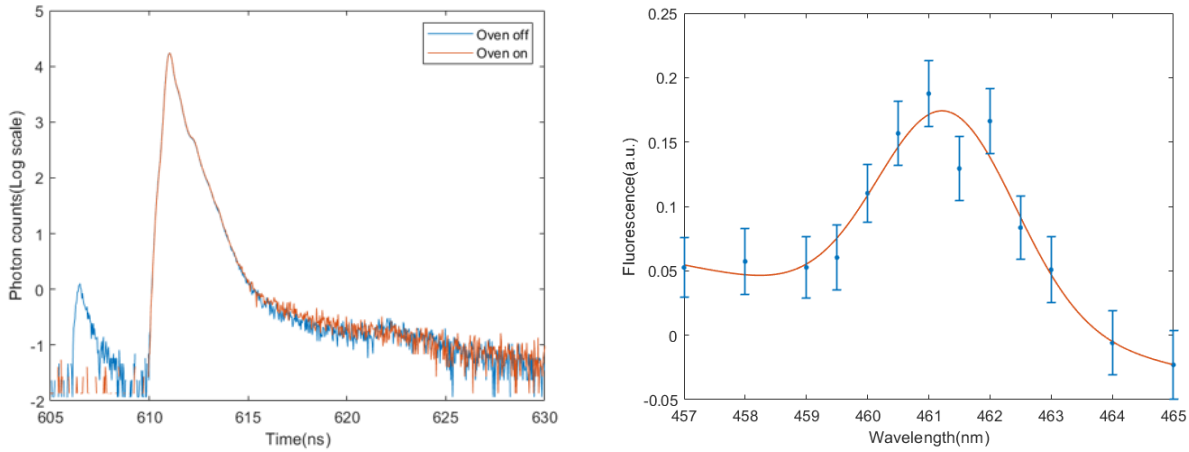

(a) Temporal signal

(b) Sr spectrum

Figure 6.5: a: Temporal Sr fluorescence signal. Laser is at around 461 nm with power 30 mW. Data taking time is 600s. Background signal (oven off) is normalized to the same peak height as the oven on signal. The difference between oven on and off at the tail corresponds to the fluorescence of Sr atoms. b: Sr spectrum. We scan the ultrafast laser and plot this difference against wavelength.

6.3 Pulse excitation probability

To calculate the density of emitters and sensitivity, we first need to figure out the excitation probability P_{e} of the relevant transition by a single pulse. The probability depends on the natural linewidth of the transition and the pulse power, rep rate, and duration.

Here is how to derive it. The laser pulse shape in time domain can be expressed as

$$E(t) = E_0 \mathrm{sech}(\frac{\pi t}{T_{\mathrm{p}}}) \tag{6.2}$$

where E is the electric field of the light and T_{p} defines the time duration of this pulse. FWHM of function in equation 6.2 is 0.84 T_{p} and the intensity FWHM is 0.56 T_{p}

$$\int_{-\infty}^{\infty} dt\, \mathrm{sech}(\frac{\pi t}{T_{\mathrm{p}}}) = T_{\mathrm{p}}, \tag{6.3}$$

$$\int_{-\infty}^{\infty} dt\, \mathrm{sech}^2(\frac{\pi t}{T_{\mathrm{p}}}) = \frac{2}{\pi} T_{\mathrm{p}}. \tag{6.4}$$

Notice that FWHM in time and frequency domain are related to each other by Fourier transformation:

$$\sigma_{\mathrm{t}} = \frac{1}{\pi \sigma_{\mathrm{f}}}. \tag{6.5}$$

Intensity of light is

$$I(t) = \frac{1}{2} c \epsilon_0 |E_0|^2 \tag{6.6}$$

where c is speed of light and ϵ_0 is vacuum permittivity. Consider Gaussian beam, the center intensity of a Gaussian beam is

$$I_{\mathrm{center}} = 2\frac{P}{\pi w_0^2} \tag{6.7}$$

where P is the power of the laser beam and w_0 is the waist. Define the pulse fluence

$$F = \frac{2\overline{P}}{f_{\mathrm{r}} \pi w_0^2} \tag{6.8}$$

where $\overline{P}$ is the time-averaged power and f_{r} is rep rate of the laser.

Suppose the system is a two-level system connected by E1 transition with natural linewidth $\gamma = 1/\tau$ and resonance optical frequency ω_{a}. The saturation intensity is

$$I_{\mathrm{sat}} = \frac{\hbar \omega_{\mathrm{a}}^3 \gamma}{12 \pi c^2}. \tag{6.9}$$

Rabi frequency is defined as

$$|\Omega| = \gamma \sqrt{\frac{I}{2 I_{\mathrm{sat}}}}. \tag{6.10}$$

The Hamiltonian under rotating frame, assuming that $\omega_{\mathrm{a}} = \omega_{\mathrm{laser}}$:

$$H(t) = -\frac{\hbar}{2} \Omega_0 \mathrm{sech}\left(\frac{\pi t}{T_{\mathrm{p}}}\right) (|g\rangle\langle e| + |e\rangle\langle g|). \tag{6.11}$$

Solution (Rosen-Zener solution [70])is

$$P_{\mathrm{e}} = \sin^2\left(\frac{\Omega_0 T_{\mathrm{p}}}{2}\right) \tag{6.12}$$

We can write the peak instantaneous optical power P_0 in terms of the time-averaged laser power $\overline{P}$

$$P_0 = \frac{\overline{P}}{f_{\mathrm{r}}\frac{2}{\pi}T_{\mathrm{p}}}. \tag{6.13}$$

So the peak intensity is

$$I_0 = 2\frac{P_0}{\pi w_0^2} = \frac{\overline{P}}{f_{\mathrm{r}} T_{\mathrm{p}} w_0^2}, \tag{6.14}$$

and the peak Rabi frequency is

$$|\Omega| = \gamma\sqrt{\frac{I}{2I_{\mathrm{sat}}}} = \sqrt{\frac{6\pi\gamma c^2\overline{P}}{\hbar w_0^2 T_{\mathrm{p}} f_{\mathrm{r}}\omega_{\mathrm{a}}^3}}. \tag{6.15}$$

So the probability is

$$P_{\mathrm{e}} = \sin^2\left(\sqrt{\frac{3\pi\gamma c^2\overline{P}T_{\mathrm{p}}}{2\hbar w_0^2 f_{\mathrm{r}}\omega_{\mathrm{a}}^3}}\right). \tag{6.16}$$

Now we can plug in numbers to calculated this probability for Sr. For Sr $^1S_0$ to $^1P_1$ transition. The laser wavelength is 461 nm ($\omega_{\mathrm{a}} = 4\times10^{15}$ rads^{-1}) with $f_{\mathrm{r}} = 1$ MHz, $T_{\mathrm{p}} = 150$ fs, $\overline{P} = 30$ mW and $w_0 = 3$ mm. The natural linewidth is $\gamma = 2\pi\times32$ MHz. So the probability is

$$P_{\mathrm{e}} = \sin^2\left(\sqrt{\frac{3\pi\times2\pi\times32\times10^6\times c^2\times0.03\times150\times10^{-15}}{2\hbar\times(0.003)^2\times1\times10^6\times(4\times10^{15})^3}}\right) = 0.0059. \tag{6.17}$$

6.4 Number of atoms detected

If the pulse excitation probability is P_{e}, the temporal signal is as

$$S(t) = NP_{\mathrm{e}} f_{\mathrm{r}} t_{\mathrm{d}}\eta\gamma e^{-\gamma t} \tag{6.18}$$

where N is the total number of emitters. f_{r} is the rep rate of the laser and t_{d} is the total detecting time. η is the total detecting efficiency. Suppose the excitation photon arriving

time is at t = 0 s. The amount of fluorescent photons arriving from t_0 to t_1 is

$$S_{\text{int}} = NP_{\text{e}}f_{\text{r}}t_{\text{d}}\eta \int_{t_0}^{t_1} \gamma e^{-\gamma t} dt = NP_{\text{e}}f_{\text{r}}t_{d}\eta \left(e^{-\gamma t_0} - e^{-\gamma t_1}\right). \tag{6.19}$$

This signal is experimentally measured by the difference of the red and blue summing over a proper time range (Figure 6.5a). Summing over the arriving time 615.2 ns to 622.7 ns, the total background counts is $S_{\text{b}} = 4995 \pm 75$ and the total signal counts is $S_{\text{s}} = 5932 \pm 84$. Then the difference is

$$\begin{aligned} S_{\text{s}} - S_{\text{b}} &= 937 \pm 112 \\ &= S_{\text{int}} \\ &= NP_{\text{e}}f_{\text{r}}t_{\text{d}}\eta \left(e^{-\gamma t_0} - e^{-\gamma t_1}\right) \\ &= N \times 67. \end{aligned} \tag{6.20}$$

With $P_{\text{e}} = 0.0059$, $f_{\text{r}} = 1$ MHz, $t_{\text{d}} = 600$ s, $\eta = \eta_{\text{a}}\eta_{\text{b}} = 0.0112 \times 0.005 = 5.6 \times 10^{-5}$, we can get the number of emitters $N = 14.0 \pm 1.7$. The Sr atomic density is

$$\rho = \frac{N}{V} = \frac{N}{\pi r^2 d} = 2.1 \times 10^6 \text{cm}^{-3} \tag{6.21}$$

where the field depth is 0.6 mm and hold diameter is 118 μm. Note here the efficiency factor comes from solid angle part $\eta_{\text{a}} = 0.0112$ and loss due to optical components and PMT detection efficiency η_{b}. It is small because we have a ND filter in front of the PMT to make sure the count rate is less than 5% of the rep rate f_{r}. The laser power and the detection efficiency are not accurate, so this is just a rough approximation of the number of Sr atoms we detected. But it at least gives us an idea of the sensitivity of this system.

6.5 Sensitivity discussion

Under current condition and approximation, we are expecting 67 total counts from one single atom in 600 s whereas the background is $S_{\text{b}} = 4995 \pm 75$ (68%). It falls in the fluctuation of the background so single Sr emitter is not or barely detectable with current apparatus.

However, if we can increase the signal to noise ratio by a factor of 2 or 3 then we may be able to see single Sr atom. One way to do this is increasing data collecting time by a factor of 4, which means taking data for 40 min. This could be a pain when we need to search for the emitter and also the emitter may not last for this long. Another idea is to use a pulse laser with longer pulse duration. Longer pulse duration means narrower linewidth, which means higher power efficiency. Basically with narrower linewidth, larger portion of the incoming photons can excite the transition. Dye laser can be used instead of the ultrafast laser. The drawback is that the dye laser is harder to align and get a clean output mode. Also the current dye laser we have is pumped at 10 Hz. This is quite slower than the ultrafast laser. Unless we can increase the efficiency by a factor of 10^5, the dye laser will be more time consuming when taking data. Other ideas are making the surface more flat, or coating the chamber with black materal like CuO to reduce scatter.

REFERENCES

[1] TM Graham, Y Song, J Scott, C Poole, L Phuttitarn, K Jooya, P Eichler, X Jiang, A Marra, B Grinkemeyer, et al. Multi-qubit entanglement and algorithms on a neutral-atom quantum computer. Nature, 604(7906):457–462, 2022.

[2] Colin D Bruzewicz, John Chiaverini, Robert McConnell, and Jeremy M Sage. Trapped-ion quantum computing: Progress and challenges. Applied Physics Reviews, 6(2):021314, 2019.

[3] Yunseong Nam, Jwo-Sy Chen, Neal C Pisenti, Kenneth Wright, Conor Delaney, Dmitri Maslov, Kenneth R Brown, Stewart Allen, Jason M Amini, Joel Apisdorf, et al. Ground-state energy estimation of the water molecule on a trapped-ion quantum computer. npj Quantum Information, 6(1):33, 2020.

[4] Johannes Majer, JM Chow, JM Gambetta, Jens Koch, BR Johnson, JA Schreier, L Frunzio, DI Schuster, Andrew Addison Houck, Andreas Wallraff, et al. Coupling superconducting qubits via a cavity bus. Nature, 449(7161):443–447, 2007.

[5] JQ You and Franco Nori. Quantum information processing with superconducting qubits in a microwave field. Physical Review B, 68(6):064509, 2003.

[6] Arkady Fedorov, Lars Steffen, Matthias Baur, Marcus P da Silva, and Andreas Wallraff. Implementation of a toffoli gate with superconducting circuits. Nature, 481(7380):170–172, 2012.

[7] Graham D Marshall, Alberto Politi, Jonathan CF Matthews, Peter Dekker, Martin Ams, Michael J Withford, and Jeremy L O'Brien. Laser written waveguide photonic quantum circuits. Optics express, 17(15):12546–12554, 2009.

[8] Brian J Smith, Dmytro Kundys, Nicholas Thomas-Peter, PGR Smith, and IA Walmsley. Phase-controlled integrated photonic quantum circuits. Optics Express, 17(16):13516–13525, 2009.

[9] Alberto Politi, Martin J Cryan, John G Rarity, Siyuan Yu, and Jeremy L O'brien. Silica-on-silicon waveguide quantum circuits. Science, 320(5876):646–649, 2008.

[10] Daniel Loss and David P DiVincenzo. Quantum computation with quantum dots. Physical Review A, 57(1):120, 1998.

[11] Ziyu Lv, Yan Wang, Jingrui Chen, Junjie Wang, Ye Zhou, and Su-Ting Han. Semiconductor quantum dots for memories and neuromorphic computing systems. Chemical reviews, 120(9):3941–4006, 2020.

[12] Thaddeus D Ladd, Fedor Jelezko, Raymond Laflamme, Yasunobu Nakamura, Christopher Monroe, and Jeremy Lloyd O'Brien. Quantum computers. nature, 464(7285):45–53, 2010.

[13] Anthony Ransford, Conrad Roman, Thomas Dellaert, Patrick McMillin, and Wesley C Campbell. Weak dissipation for high-fidelity qubit-state preparation and measurement. Physical Review A, 104(6):L060402, 2021.

[14] L Armelao, S Quici, F Barigelletti, G Accorsi, G Bottaro, M Cavazzini, and E Tondello. Design of luminescent lanthanide complexes: From molecules to highly efficient photoemitting materials. Coordination Chemistry Reviews, 254(5-6):487–505, 2010.

[15] Daniel N Woodruff, Richard EP Winpenny, and Richard A Layfield. Lanthanide single-molecule magnets. Chemical reviews, 113(7):5110–5148, 2013.

[16] Jun-Liang Liu, Yan-Cong Chen, and Ming-Liang Tong. Symmetry strategies for high performance lanthanide-based single-molecule magnets. Chemical Society Reviews, 47(7):2431–2453, 2018.

[17] Kasper S Pedersen, Ana-Maria Ariciu, Simon McAdams, Høgni Weihe, Jesper Bendix, Floriana Tuna, and Stergios Piligkos. Toward molecular 4f single-ion magnet qubits. Journal of the American Chemical Society, 138(18):5801–5804, 2016.

[18] Dmitry Budker and Michael Romalis. Optical magnetometry. Nature physics, 3(4):227–234, 2007.

[19] Vishal Shah, Svenja Knappe, Peter DD Schwindt, and John Kitching. Subpicotesla atomic magnetometry with a microfabricated vapour cell. Nature Photonics, 1(11):649–652, 2007.

[20] IK Kominis, TW Kornack, JC Allred, and Michael V Romalis. A subfemtotesla multichannel atomic magnetometer. Nature, 422(6932):596–599, 2003.

[21] JC Allred, RN Lyman, TW Kornack, and Michael V Romalis. High-sensitivity atomic magnetometer unaffected by spin-exchange relaxation. Physical review letters, 89(13):130801, 2002.

[22] David Parker, Elizaveta A Suturina, Ilya Kuprov, and Nicholas F Chilton. How the ligand field in lanthanide coordination complexes determines magnetic susceptibility anisotropy, paramagnetic nmr shift, and relaxation behavior. Accounts of Chemical Research, 53(8):1520–1534, 2020.

[23] GE Buono-Core, H Li, and B Marciniak. Quenching of excited states by lanthanide ions and chelates in solution. Coordination Chemistry Reviews, 99:55–87, 1990.

[24] Jihyun An, Chad M Shade, Demetra A Chengelis-Czegan, Stephane Petoud, and Nathaniel L Rosi. Zinc-adeninate metal- organic framework for aqueous encapsulation and sensitization of near-infrared and visible emitting lanthanide cations. Journal of the American Chemical Society, 133(5):1220–1223, 2011.

[25] Lorenzo Di Bari, Guido Pintacuda, and Piero Salvadori. Stereochemistry and near-infrared circular dichroism of a chiral yb complex. Journal of the American Chemical Society, 122(23):5557–5562, 2000.

[26] H Wang, PL Gould, and WC Stwalley. Photoassociative spectroscopy of ultracold k 39 atoms in a high-density vapor-cell magneto-optical trap. Physical Review A, 53(3):R1216, 1996.

[27] N Malossi, MM Valado, S Scotto, P Huillery, P Pillet, D Ciampini, E Arimondo, and O Morsch. Full counting statistics and phase diagram of a dissipative rydberg gas. Physical Review Letters, 113(2):023006, 2014.

[28] Ashley J Shin, Changling Zhao, Yi Shen, Claire E Dickerson, Barry Li, Daniel Bím, Timothy L Atallah, Paul H Oyala, Lianne K Alson, Anastassia N Alexandrova, et al. Toward liquid cell quantum sensing: Ytterbium complexes with ultra-narrow absorption. 2022.

[29] Donald R Scott and Jean B Allison. Solvent glasses for low temperature spectroscopic studies. The Journal of Physical Chemistry, 66(3):561–562, 1962.

[30] Y Lu and Alfons Penzkofer. Absorption behaviour of methanolic rhodamine 6g solutions at high concentration. Chemical physics, 107(2-3):175–184, 1986.

[31] Kasper S Pedersen, Jan Dreiser, Høgni Weihe, Romain Sibille, Heini V Johannesen, Mikkel A Sørensen, Bjarne E Nielsen, Marc Sigrist, Hannu Mutka, Stephane Rols, et al. Design of single-molecule magnets: insufficiency of the anisotropy barrier as the sole criterion. Inorganic chemistry, 54(15):7600–7606, 2015.

[32] Matteo Atzori, Kais Dhbaibi, Haiet Douib, Maxime Grasser, Vincent Dorcet, Ivan Breslavetz, Kévin Paillot, Olivier Cador, Geert LJA Rikken, Boris Le Guennic, et al. Helicene-based ligands enable strong magneto-chiral dichroism in a chiral ytterbium complex. Journal of the American Chemical Society, 143(7):2671–2675, 2021.

[33] PO Petit, J Petit, Ph Goldner, and B Viana. Inhomogeneous broadening of optical transitions in yb: Cayalo4. Optical Materials, 30(7):1093–1097, 2008.

[34] A Kirmiz, DJ Saiki, and MP Augustine. Cavity ring-down observation of yb3+ optical absorption in room temperature solution. Spectrochimica Acta Part A: Molecular and Biomolecular Spectroscopy, 75(4):1211–1217, 2010.

[35] Adam Gorczyński, Dawid Marcinkowski, Maciej Kubicki, Marta Löffler, Maria Korabik, Mirosław Karbowiak, Piotr Wiśniewski, Czesław Rudowicz, and Violetta Patroniak. New field-induced single ion magnets based on prolate er (iii) and yb (iii) ions: tuning the energy barrier u eff by the choice of counterions within an n 3-tridentate schiff-base scaffold. Inorganic Chemistry Frontiers, 5(3):605–618, 2018.

[36] Karl A Gschneidner, LeRoy Eyring, GR Choppin, and GH Lander. Handbook on the physics and chemistry of rare earths: Volume 18: Lanthanides/actinides: Chemistry. 1994.

[37] Jonathan M Kindem, Andrei Ruskuc, John G Bartholomew, Jake Rochman, Yan Qi Huan, and Andrei Faraon. Control and single-shot readout of an ion embedded in a nanophotonic cavity. Nature, 580(7802):201–204, 2020.

[38] Robert C Hilborn. Einstein coefficients, cross sections, f values, dipole moments, and all that. American Journal of Physics, 50(11):982–986, 1982.

[39] Pavel Rynkun, Per Jönsson, Gediminas Gaigalas, and C Froese Fischer. Energies and e1, m1, e2, and m2 transition rates for states of the 2s22p3, 2s2p4, and 2p5 configurations in nitrogen-like ions between f iii and kr xxx. Atomic Data and Nuclear Data Tables, 100(2):315–402, 2014.

[40] Timothy D Dunbar, William L Warren, Bruce A Tuttle, Clive A Randall, and Yoed Tsur. Electron paramagnetic resonance investigations of lanthanide-doped barium titanate: dopant site occupancy. The Journal of Physical Chemistry B, 108(3):908–917, 2004.

[41] Atanu Dey, Pankaj Kalita, and Vadapalli Chandrasekhar. Lanthanide (iii)-based single-ion magnets. ACS omega, 3(8):9462–9475, 2018.

[42] Bernadine M Flanagan, Paul V Bernhardt, Elmars R Krausz, Stefan R Lüthi, and Mark J Riley. A ligand-field analysis of the trensal (h3trensal= 2, 2 ‘, 2 “-tris (salicylideneimino) triethylamine) ligand. an application of the angular overlap model to lanthanides. Inorganic chemistry, 41(20):5024–5033, 2002.

[43] Timothy L Atallah, Anthony V Sica, Ashley J Shin, Hannah C Friedman, Yaniv K Kahrobai, and Justin R Caram. Decay-associated fourier spectroscopy: visible to shortwave infrared time-resolved photoluminescence spectra. The Journal of Physical Chemistry A, 123(31):6792–6798, 2019.

[44] Martín Amoza, Silvia Gómez-Coca, and Eliseo Ruiz. Magnetic anisotropy in yb iii complex candidates for molecular qubits: a theoretical analysis. Physical Chemistry Chemical Physics, 23(3):1976–1983, 2021.

[45] Loïc Rondin, Jean-Philippe Tetienne, Thomas Hingant, Jean-François Roch, Patrick Maletinsky, and Vincent Jacques. Magnetometry with nitrogen-vacancy defects in diamond. Reports on progress in physics, 77(5):056503, 2014.

[46] Stefania Castelletto and Alberto Boretti. Silicon carbide color centers for quantum applications. Journal of Physics: Photonics, 2(2):022001, 2020.

[47] Peter DD Schwindt, Svenja Knappe, Vishal Shah, Leo Hollberg, John Kitching, Li-Anne Liew, and John Moreland. Chip-scale atomic magnetometer. Applied Physics Letters, 85(26):6409–6411, 2004.

[48] Francesco Casola, Toeno Van Der Sar, and Amir Yacoby. Probing condensed matter physics with magnetometry based on nitrogen-vacancy centres in diamond. Nature Reviews Materials, 3(1):1–13, 2018.

[49] Christian Degen. Microscopy with single spins. Nature nanotechnology, 3(11):643–644, 2008.

[50] Patrick Appel. Scanning nanomagnetometry: Probing magnetism with single spins in diamond. PhD thesis, University_of_Basel, 2017.

[51] Christopher J Foot. Atomic physics, volume 7. OUP Oxford, 2004.

[52] Thaned Pruttivarasin and Hidetoshi Katori. Compact field programmable gate array-based pulse-sequencer and radio-frequency generator for experiments with trapped atoms. Review of Scientific Instruments, 86(11):115106, 2015.

[53] Grant R Fowles. Introduction to modern optics. Courier Corporation, 1989.

[54] Donald J Metz and Althea Glines. Density, viscosity, and dielectric constant of tetrahydrofuran between-78 and 30. degree. The Journal of Physical Chemistry, 71(4):1158–1158, 1967.

[55] Daniel T Bowron, John L Finney, and Alan K Soper. The structure of liquid tetrahydrofuran. Journal of the American Chemical Society, 128(15):5119–5126, 2006.

[56] Guo-Zhu Zhu, Debayan Mitra, Benjamin L Augenbraun, Claire E Dickerson, Michael J Frim, Guanming Lao, Zack D Lasner, Anastassia N Alexandrova, Wesley C Campbell, Justin R Caram, et al. Functionalizing aromatic compounds with optical cycling centres. Nature chemistry, 14(9):995–999, 2022.

[57] Leonard J Marabella. Molecular motion and band shapes in liquids. Applied Spectroscopy Reviews, 7(2):313–355, 1973.

[58] Anne B Myers. Molecular electronic spectral broadening in liquids and glasses. Annual review of physical chemistry, 49(1):267–295, 1998.

[59] Indrek Renge. Mechanisms of solvent shifts, pressure shifts, and inhomogeneous broadening of the optical spectra of dyes in liquids and low-temperature glasses. The Journal of Physical Chemistry A, 104(32):7452–7463, 2000.

[60] Ryuichi Ito, Yuuki Funamoto, Nobuhiro Ohta, and Toshifumi Iimori. Electroabsorption spectroscopy of electronic transition for room-temperature ionic liquid molecules dispersed in a polymer matrix. Chemical Physics, 456:1–7, 2015.

[61] Martin Liess, S Jeglinski, ZV Vardeny, Masanori Ozaki, K Yoshino, Y Ding, and T Barton. Electroabsorption spectroscopy of luminescent and nonluminescent π-conjugated polymers. Physical Review B, 56(24):15712, 1997.

[62] Dennis H Oh, Mitsuru Sano, and Steven G Boxer. Electroabsorption (stark effect) spectroscopy of mono-and biruthenium charge-transfer complexes: measurements of changes in dipole moments and other electrooptic properties. Journal of the American Chemical Society, 113(18):6880–6890, 1991.

[63] Stephen D Fried, Sayan Bagchi, and Steven G Boxer. Extreme electric fields power catalysis in the active site of ketosteroid isomerase. Science, 346(6216):1510–1514, 2014.

[64] Gerold U Bublitz and Steven G Boxer. Stark spectroscopy: applications in chemistry, biology, and materials science. Annual review of physical chemistry, 48(1):213–242, 1997.

[65] Shijie Deng and Paula L Diaconescu. A switchable dimeric yttrium complex and its three catalytic states in ring opening polymerization. Inorganic Chemistry Frontiers, 8(8):2088–2096, 2021.

[66] Ivan Kozyryev and Nicholas R. Hutzler. Precision measurement of time-reversal symmetry violation with laser-cooled polyatomic molecules. Phys. Rev. Lett., 119:133002, Sep 2017.

[67] Ivan Kozyryev, Louis Baum, Kyle Matsuda, Boerge Hemmerling, and John M. Doyle. Radiation pressure force from optical cycling on a polyatomic molecule. Journal of Physics B: Atomic, Molecular and Optical Physics, 49(13):134002, June 2016.

[68] Ivan Kozyryev, Louis Baum, Kyle Matsuda, and John M. Doyle. Proposal for laser cooling of complex polyatomic molecules. ChemPhysChem, 17(22):3641–3648, 2016.

[69] Han Guo, Claire E Dickerson, Ashley J Shin, Changling Zhao, Timothy L Atallah, Justin R Caram, Wesley C Campbell, and Anastassia N Alexandrova. Surface chemical trapping of optical cycling centers. Physical Chemistry Chemical Physics, 23(1):211–218, 2021.

[70] Nathan Rosen and Clarence Zener. Double stern-gerlach experiment and related collision phenomena. Physical Review, 40(4):502, 1932.